POLITECNICO
MILANO 1863

SCUOLA DI INGEGNERIA INDUSTRIALE
E DELL'INFORMAZIONE

Geometry optimization of superconducting nanowire single photon detectors (SNSPDs) towards background-free X-ray detection

Tesi di Laurea Magistrale in
Physics Engineering

Author: **Alessandro Cerioni**

Student ID: 970642
Advisor: Prof. Gianluca Valentini
Co-advisors: Stephan Steinhauer Ulrich Vogt Val Zwiller
Academic Year: 2022-23

Abstract

X-ray detectors, exhibiting high sensitivity, are relevant for a considerable number of applications in physics, medicine and other scientific fields. Superconducting nanowire single-photon detectors (SNSPDs), which have proven outstanding performances in the infrared (IR) regime, can represent good candidate for the X-ray range as well. A previous work, analysing the soft X-ray response of SNSPDs, confirms such qualities, especially in terms of detected counts and efficiency. It also argues that the major counting detection contribution is to be ascribed to the substrate scintillation, which falls in the visible-infrared (VIS-IR) regime. The objective of this work is to optimize the width and thickness of the nanowire in order to suppress infrared (IR) counts for wavelengths greater than 850 nm. Niobium Titanium Nitride (NbTiN) SNSPDs on top of a SiO_2 substrate is employed to be consistent with the reference work. Geometry optimization is performed using a Python toolbox with built-in functions to realize meandering structures. Results show that widths above 100 nm do not detect any infrared (IR) light and, if this devices are used in a soft X-ray experiment, it should result in a dramatic reduction of the final counts.

Keywords: X-ray SNSPDs, IR suppression in SNSPDs

Abstract in lingua italiana

I rivelatori di raggi X, che mostrano un'elevata sensibilità, sono rilevanti per un numero considerevole di applicazioni in fisica, medicina e altri campi scientifici. Il rivelatore superconduttori a nanofilo, capace di rilevare il singolo fotone (SNSPD) e che ha dimostrato prestazioni eccezionali nel regime dell'infrarosso (IR), può rappresentare un buon candidato anche per la gamma dei raggi X. In un lavoro precedente, analizzando la risposta ai raggi X molli degli SNSPD, si confermano tali qualità, soprattutto in termini di conteggi rilevati ed efficienza. Si sostiene inoltre che il principale contributo di rilevamento di tale conteggio è da attribuire alla scintillazione del substrato, che rientra nel regime del visibile-infrarosso (VIS-IR). L'obiettivo di questo lavoro è ottimizzare la larghezza e lo spessore del nanofilo al fine di sopprimere i conteggi degli infrarossi (IR) per lunghezze d'onda maggiori di 850 nm. Per essere coerenti con il lavoro di riferimento, vengono impiegati SNSPDs di niobio e nitruro di titanio (NbTiN) su un substrato di SiO_2 (Quarzo). L'ottimizzazione della geometria viene eseguita utilizzando un toolbox Python con funzioni integrate per realizzare strutture a meandri. I risultati mostrano che larghezze superiori a 100 nm non rilevano alcuna luce infrarossa (IR) e si ritiene, che se questi dispositivi venissero utilizzati in un esperimento di raggi X morbidi, si avrebbe una drastica riduzione dei conteggi finali.

Parole chiave: Rilevamento raggi X in SNSPDs, soppressione luce infrarossa per applicazioni riguardanti SNSPDs

Contents

1 | Introduction

Superconducting nanowire single-photon detectors exhibit indispensable qualities when dealing with quantum photonics and single-photon oriented applications. Near-unity detection efficiency for a wide spectral range, low dark counts, short dead times, pico-second time resolution (time jitter), high maximum count rates and large active areas allow them to exceed many devices used for analogous purposes such as single-photon avalanche diode (SPAD) and photomultiplier tubes(PMTs). Nevertheless, they do present some limitations which are far from being overcome, as the cryogenic temperatures needed to preserve superconducting state.

1.1. Application

The wide spectral detection window shown by superconductor nanowire single-photon detectors, make these devices suitable for a great deal of different applications. Thanks to both direct and indirect detection mechanisms, which will be discussed later, SNSPD devices can detect photons from mid-infrared (10μm) [1] infrared up to X-ray ranges[2]. These different detection mechanism can be exploited for a variety of purposes and applications. In the following few of them are listed.

1.1.1. LIDAR

LIDAR, light detection and ranging, is a remote measurement technique used to investigate distant object and parameters associated to the atmosphere or even vegetation. This technique and its characteristics depend mainly on the kind of detector they employ making SNSPDs one of the best candidate for this purpose due to their high performance, especially in the IR range [3].

1.1.2. OTDR

Optical time domain reflectometer is an opto-electronic instrument that sends a series of optical pulses in an optical fiber and collects information from scattered and reflected

photons at the other end of the fiber. They are usually employed in combination with APDs (avalanche photodiode) as reported in [4] allowing for good sensing distance and resolution. However, if SNSPDs are used, they can reach a maximum sensing distance of 246.8 km, at a two-point resolution of 0.1 km outperforming the previous ones [5].

1.1.3. Medical applications

The use of SNSPDs in medical applications is of great interest as they can greatly improve the efficiency and resolution of the tools they are employed in. Positron emission tomography (PET) is a functional imaging technique that uses radioactive substances, known as radiotracers, to measure changes in metabolic processes and other physiological activities. It is generally used in combination with x-ray computed tomography (CT) or magnetic resonance (MR) which greatly improves the quality of the images. It is argued that the high time resolution of SNSPDs will allow for 10 ps (Time of flight) TOF-PET [6]. SNSPDs' great sensitivity in IR detection make them also suitable for imaging deep into biological tissue and allow for exploitation of several energy windows around the 1.3 μm or 2.1 μm. Indeed they can be used to detect the weak emission from oxygen singlet at 1270 nm [7].

1.2. State of the arts

As far as detection efficiency is concerned, it is worth mentioning two examples where SDE (system detection efficiency) reached almost unity. In [8] the authors show an all-dielectric layered stack and fiber coupling package in order to achieve 98 $\pm$ 0.5% using a highly attenuated 1550 nm continuous-wave laser. In [9] a novel fabrication technique led to membrane-based devices which, employing a metal reflector, showed $99.5+0.5-2.07\%$ SDE at 1350 nm with 32 ps timing jitter (using a room-temperature amplifier), and other detectors in the same batch showed (94–98)% SDE at 1260–1625 nm with 15–26 ps timing jitter (using cryogenic amplifiers). Time jitter is indeed one of the most relevant parameters, representing the time delay between single-photon impinging on the detector and subsequent electrical detection signal. In addition to detector jitter, several factors contribute to the overall system jitter: the laser synchronization, electrical noise and dispersion of light within the fiber. The most striking result was obtained in 2021 when the lowest time jitter of < 3 ps was reported with short NbN nanowires. [7]. A main source of noise in light detection systems are dark counts, i.e., unwanted detection events generated under no illumination conditions. Dark counts result from current-assisted unbinding of vortex-antivortex pairs [10] and from black-body radiation [11] inducing

absorption of photons and thus the creation of a hotspot. Dark counts can be as low as 10^{-4} Hz with a bandwidth up to 100 GHz [10].

1.3. Thesis objective

The present work is intended to optimize the width of the Niobium Titanium Nitride (NbTiN) nananowire in order to suppress IR counts for light of wavelength greater than 850 nm. This work preludes and further investigates the X-ray response of SNSPDs studied in [2]. Here, it is argued that the major detection event mechanism in these devices, in the X-ray range, is to be ascribed to the substrate scintillation, laying in IR regime. Although X-ray illumination was not carried out for delays in the set-up of the laboratory, simulations of the substrate scintillations with $\lambda = 850$ nm are performed. It is found that widths above 100 nm do not detect any infrared (IR) light. Thus, if this devices are used in a soft X-ray experiment, it should result in a dramatic reduction of the detected counts. A second objective concerns the interaction analysis of devices at nanometric distance between them. The structure, referred to as "interleaved structure", consists of two superconducting nanowires, one placed internally with respect to the other one. The idea is to flood illuminate the overall structure while operating in detection mode (thus applying a dc bias current) just one of the two devices. Results show that the number of detected counts is unchanged for such devices, suggesting that no quantum interaction mechanism ("cross-talk") arises.

1.4. Thesis outline

Chapter two introduces the coding program PHIDL with some of the different designs that have been employed in the analysis of SNSPDs. **Chapter three** describes accurately the fabrication steps necessary to obtain such devices. In **Chapter four** fundamental aspects of superconductivity are introduced. In **Chapter five** detection mechanisms, useful parameters and the most relevant elements concerning system functioning are given. In **Chapter six** the results of the article this thesis work refers to are reported. In **Chapter seven** the results of this project and their interpretations are given. Finally **Chapter eight** outlines possible future developments of this work.

2 | SNSPDs design

This chapter deals with the creation of designs suitable for microfabrication experiments. The reasons for the particular shape of SNSPD devices is also explained. Many software can be employed for the implementation of SNSPD designs. The most elementary ones rely on merging standard geometries to output a more complex layout. Although they are easy to operate with, they do not allow for patterning challenging shapes, as the meandering ones that are usually found in SNSPDs. An example is Klayout, which is a graphic tool mostly used to visualize .gds extension designs or to create basic structures. To implement more demanding designs, script-based layouting software are needed such as Matlab and PHIDL. The first one is a dynamic programming environment where, to create geometric configurations, it is necessary to develop a script in Matlab programming language. Same reasoning applies to PHIDL which is a python based program. Both these tools generates .gds files which are then fed to Beamer, a program which converts, corrects and breaks down the code in a fashion suitable for the electron beam lithography tool. Both Matlab and PHIDL are considered to be highly efficient, since with a code based program, it is less time consuming to develop a layout consisting of several structures with analogous characteristics. In addition, PHIDL internally contains many built-in functions associated with geometries and structures related to SNSPDs. This feature makes PHIDL the most intuitive program to be used allowing for reduction of coding errors too. The user can design complex 2D geometries for nanolithography and device design [12]. Indeed, Included are functions like snspd(), intended to create superconducting nanowire single-photon detectors using optimized curves, which reduce the problem of superconducting "current crowding". The latter one refers to geometry induced reduction in the critical current of the device (this quantity will be deeply discussed in the following). Same reasoning applies for the function optimal.step() [13].

Figure 2.1 shows the design of a representative SNSPD with length l=250 μm and width w=100 nm. The specific choice for these orders of magnitude will be discussed later on, here just the picked geometry is analysed. The squared pads, of 150 μm side length, are needed to connect the device, through Aluminum wire bonding, with a printed circuit board. in Figure 2.2, the layout is presented in magnified view to show the active detector

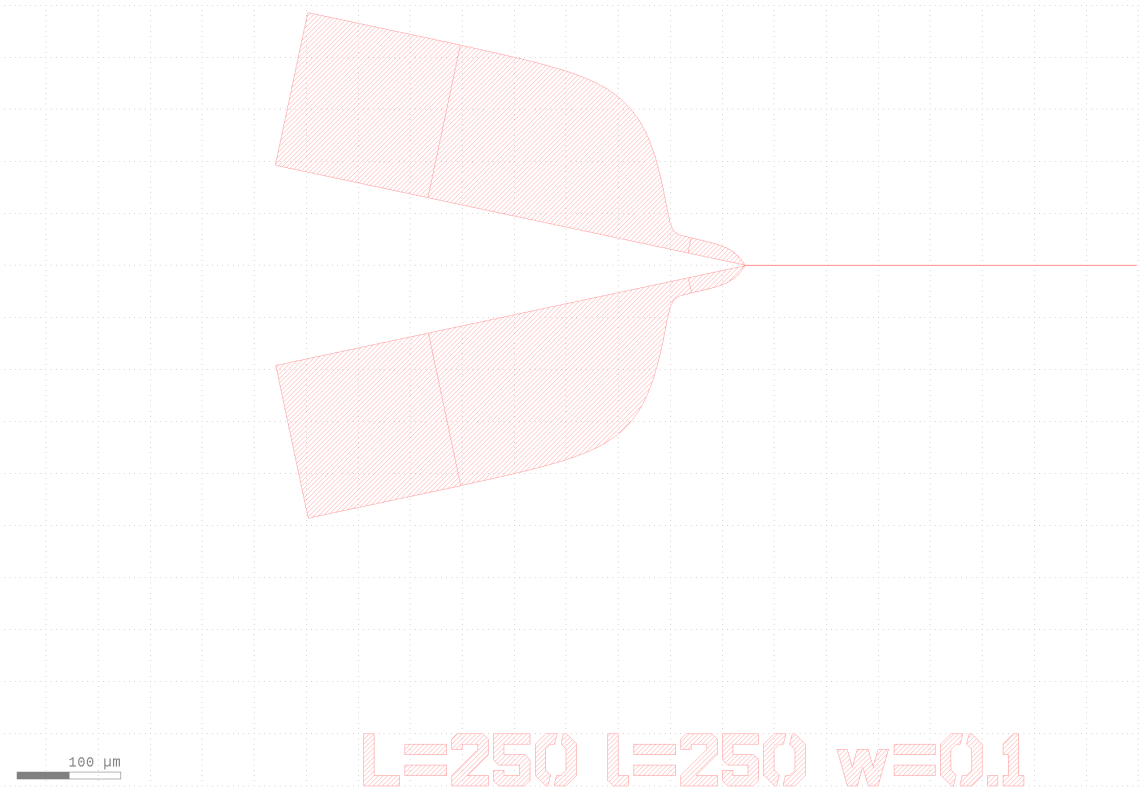

Figure 2.1: Example Design

region and the turnaround geometry. the structure has a fill factor of 0.5, meaning that the space in between the meander, shown in figure 2.2, is of the same width as that of the nanowire. In between, the pads and the meandering nanowire are connected with the function optimal.step(). The latter one gradually reduces the cross section (lateral size) of the device from the pad dimension to that of the nanowire. It does so, computing the minimum length to prevent the current-crowding issue. [13]. Starting from the above geometry many configurations of different SNSPDs with different lengths and widths were implemented see Fig.2.4. The goal of having neighboring nanowires with different widths will allow to distinguish between infrared and X-ray counts as in the first case relevantly more detection events are expected.

[13]. This tool allows for the realization of other challenging designs as the "interleaved" geometry which is implemented in order to investigate if "cross-talk" is present between adjacent superconducting structures. The shape is shown in Fig.2.3. Indeed, as the distance between the structure is in the nm order of magnitude, it is relevant to see if any quantum behavior arises, making the two structures interact with each other. A coding example of an interleaved design is reported in Appendix A.
A final example of the complex geometries to be designed which can be employed to have

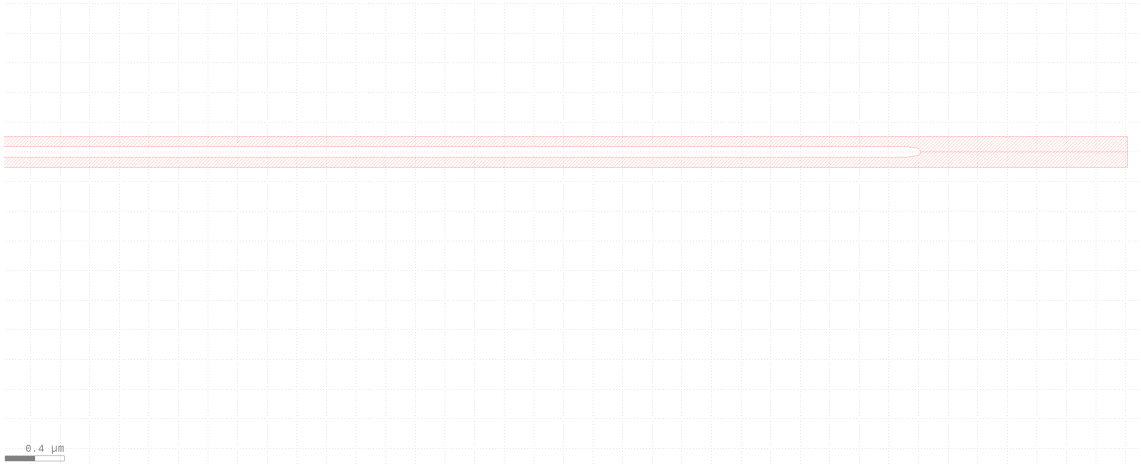

Figure 2.2: Meandering nanowire, usually referred to as "hairpin"

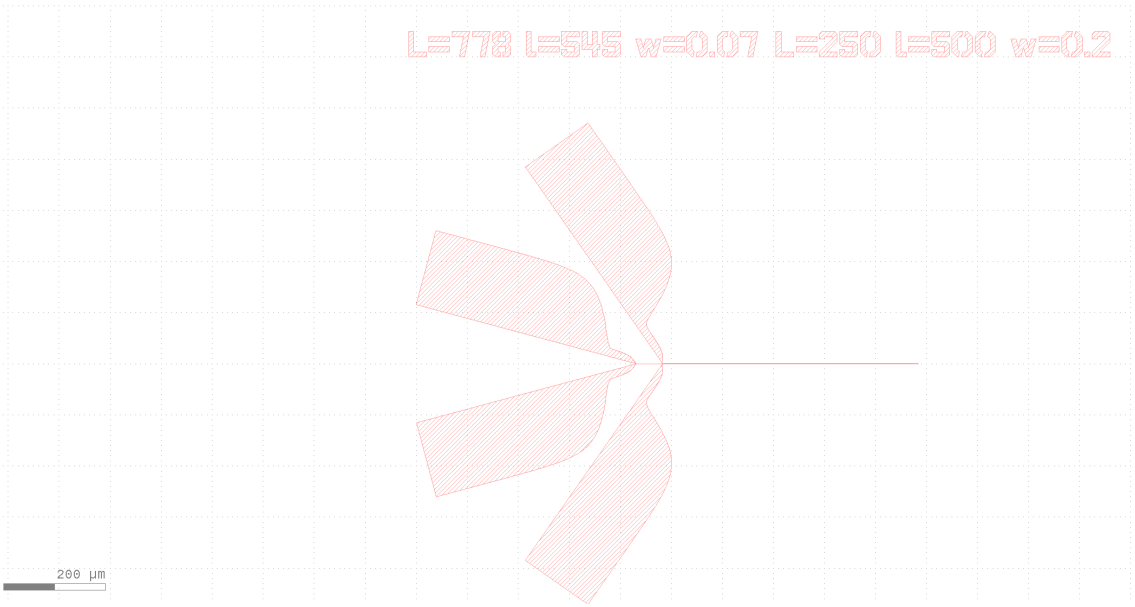

Figure 2.3: Interleaved structure

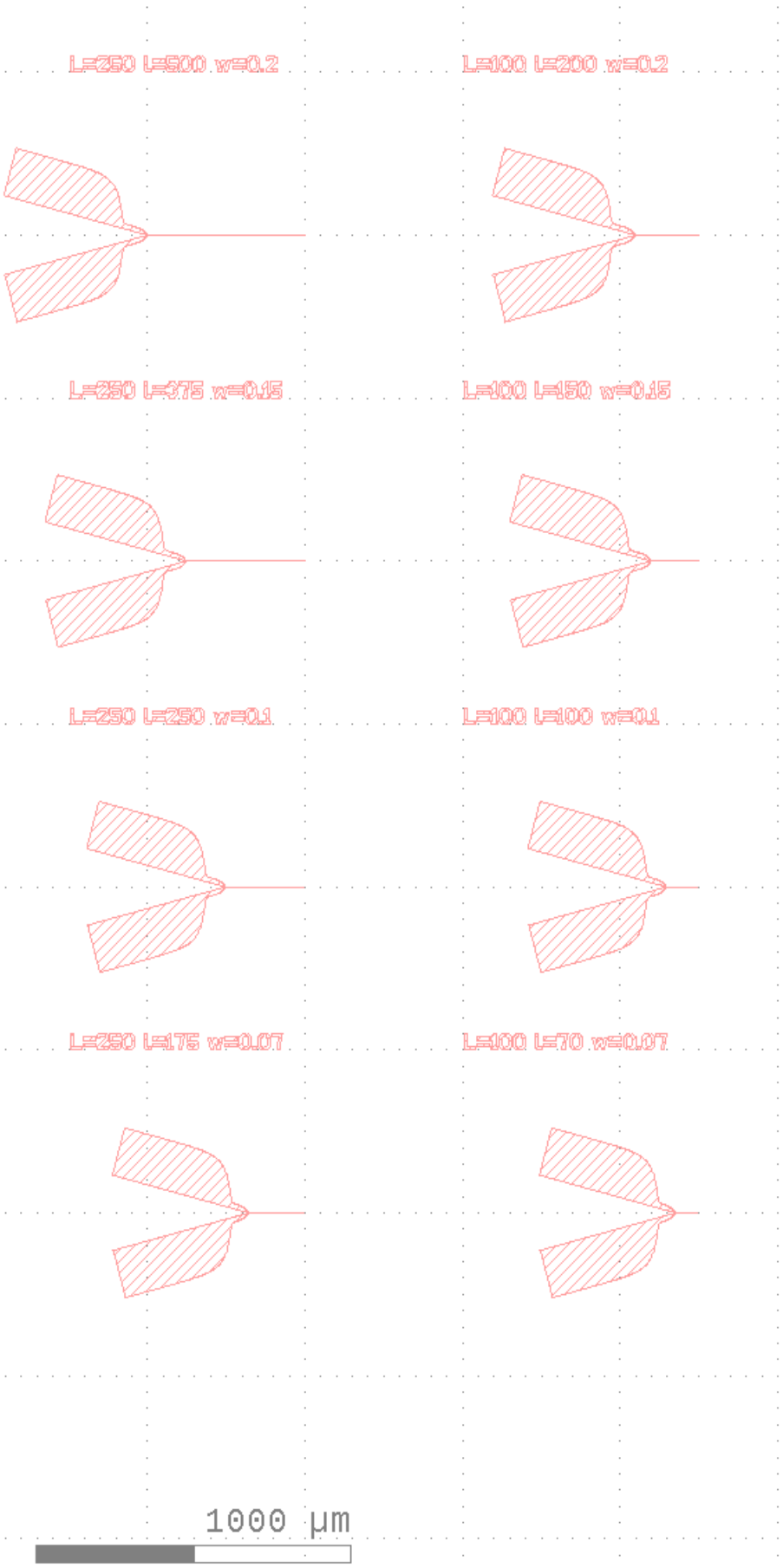

Figure 2.4: Designs for the second experiment

a good trade-off between the fill factor of the structure and reduction in current crowding (usually appearing in abruptly curved geometries) is the one reported in Fig.2.5.

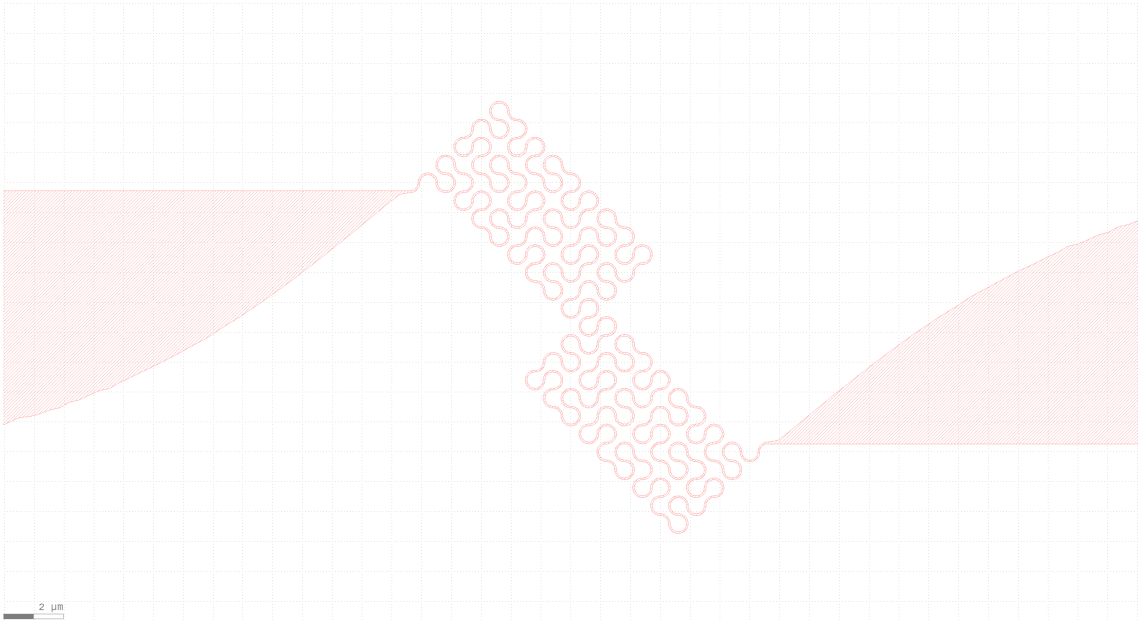

Figure 2.5: Peano like structure

3 | Fabrication of SNSPDs

This chapter deals with the fabrication process pursued to produce superconducting nanowire single-photon detectors. SNSPDs, as shown in 3.1, are fabricated by patterning of a superconducting thin film. The implementation of a 12 nm film of Niobium Titanium Nitride ($Nb_{0.4}Ti_{0.6}N$) on a SiO_2 (Quartz) layer of 270 nm is obtained through a series of steps of a standard procedure. Figure 3.1 shows a graphic overview of how each step specifically contributes to the fabrication of such devices. Starting from a SiO_2 layer on top of a silicon substrate, a thin film of Niobium Titanium Nitride with the previously reported concentrations is deposited, through DC sputtering. The sample is then spin coated with negative resist and subsequently baked to make it suitable for electron beam lithography. A negative resist is a material whose chemical bond toughen upon interaction with an electron beam. The development then removes the regions that were not hit by the electron beam. Finally, the etching process transfers the pattern into the layer beneath through both a mechanical and chemical action.

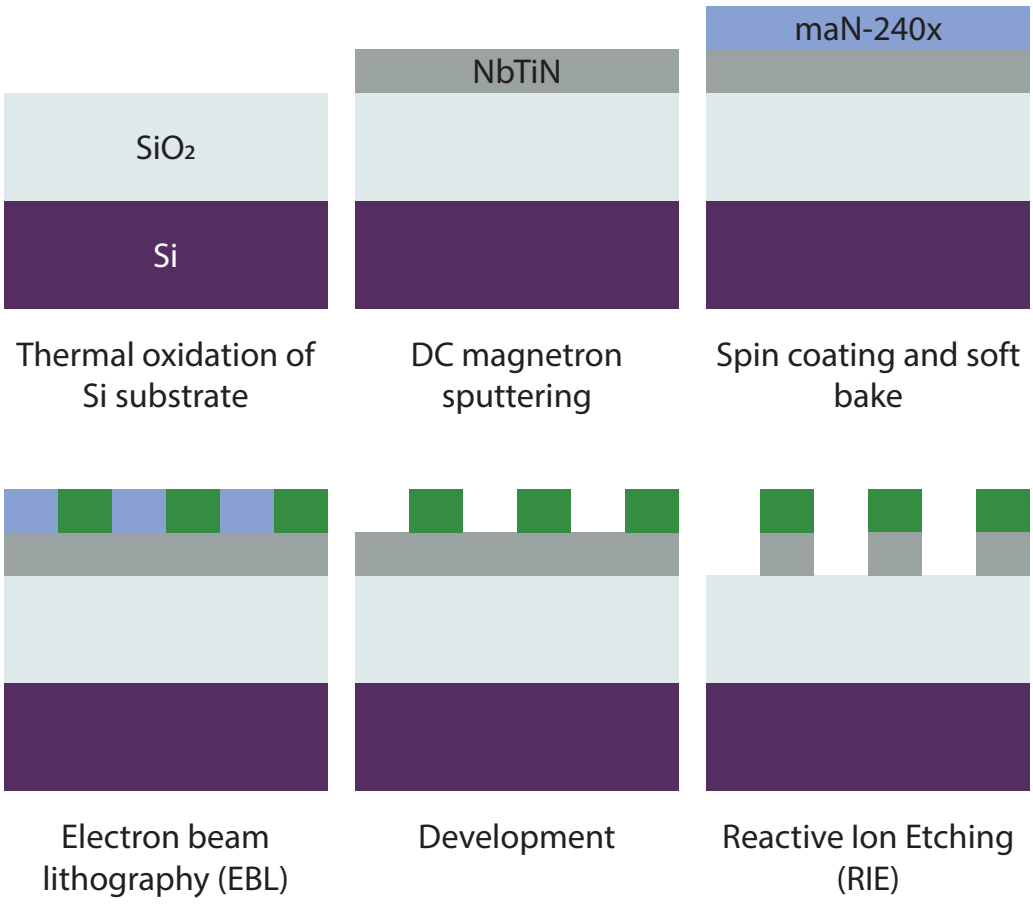

Figure 3.1: Schematic of the fabrication process

3.1. DC magnetron sputtering

The deposition of ($Nb_{0.6}Ti_{0.4}N$) on a SiO_2 substrate of 270 nm (which is on a 250 μm Si layer) is performed with the AJA II ATC2200 sputtering system shown in Fig. 3.3. Reactive co-sputtering from separate Nb and Ti targets at room temperature is used. The magnetron sources operating at, respectively, DC bias of 120 W and a RF bias of 240 W for Nb and Ti, are in an atmosphere of Ar and N_2 with a pressure of 3 mTorr and Ar to N_2 ratio of 10:1[14]. The substrate are placed on a rotating sample holder needed to maximize homogeneity of the deposition. The process relies on Argon ions (Ar+) in the discharge plasma which accelerated by electrical fields hit the negatively biased target, ejecting typically one target atom as shown in Fig 3.2. The ejected atoms are then transported to the substrate wafers. A major advantage of the system is that it is possible to control the relative concentration of Nb an Ti, as it is reported in Fig.3.4 [15].

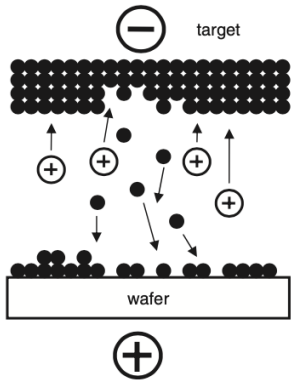

Figure 3.2: Sputtering process [16]

Figure 3.3: AJA II ATC2200 sputtering system

3.2. Spin coating with negative resist and post-bake

For microfabrication and nanofabrication processes the use of either photosensitive and electron-sensitive resist is necessary. The resist is a polymer generally made of three parts: 1-**Base resin** which determines the mechanical and thermal properties; 2-**Photoactive Compound** which determines sensitivity to radiation; 3-**Solvent** which controls viscosity. In this case, as electron beams are used to pattern the chip thin film an electron sensitive resist must be employed. The reason is that electrons can allow for smaller geometries generation, as they do not suffer from diffraction limitation, leading to nanometric featured devices. Resist are further distinguished between positive and negative. Positive resist undergo bonds weakening upon exposure while negative resist toughen their chemical

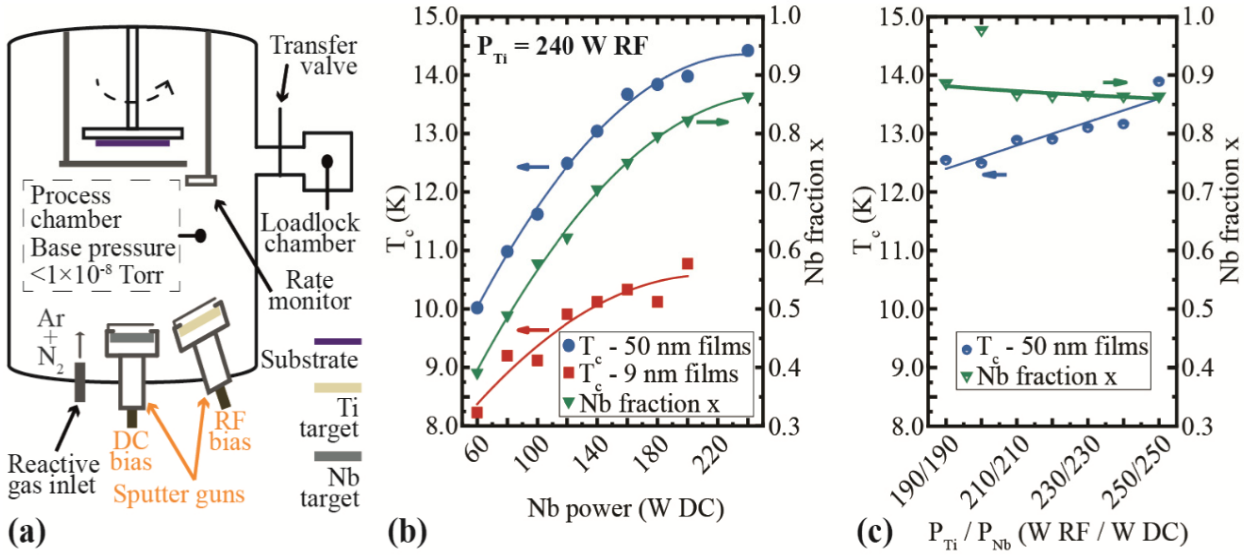

Figure 3.4: (a) Schematics of the sputtering chamber. (b) Critical temperature Tc and Nb fraction x in the alloy NbxTi1-xN vs. Nb sputtering power. The power applied to the Ti target was kept constant at 240 W RF for all film depositions. (c) Critical temperature Tc and Nb fraction x vs. sputtering power for a constant power ratio. The lines are a guide to the eye[15]

bonds. This implies that during the development process, positive resists will lose the exposed regions resulting in engraved features while negative resists will preserve the exposed parts resulting in emerging features. Therefore, a negative resist, namely Man-2401, is employed as we want to fabricate nanowires, which are structure emerging from the underneath layer.

To obtain a layer of resist of 100 nm it is necessary to refer to the curve relating the thickness and the revolutions per minute shown of that specific resist as reported in Fig. 3.5.

A spin speed = 4000 rpm (revolutions per minute) is chosen in order to have a resist layer thickness of about 100 nm. Such thickness of the resist layer is a common choice whenever dealing with nanometric featured devices. In fact, very thin resist layers allows the defocus plane (the plane at which the electron beam is focused) to be as close as possible to the interface between the superconducting material and its substrate. Such condition is necessary to achieve nm resolution of electron beam lithography. To ensure good quality of spin coated films, it is important to have smooth and clean surfaces. For the removal of larger particulates (dust, hair etc.) light bursts from an N_2 gun are employed. In addition, in order to help the resist apply on top of the quartz layer the adhesion promoter AR 300-80 can be used.

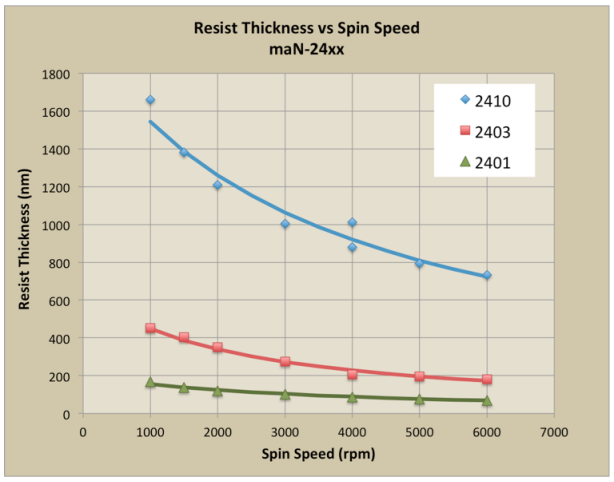

Figure 3.5: Resist thickness vs rpm

The two main parts of the procedure consist of:
a. 60 s spinning at 4000 rpm (ramp 500 rpm/s).
b. 90 s on top of the hotplate at 115 °C. Resist post-spin bake is necessary as it completes the photopolymerization process. In addition, It enhances the diffusion of photogenerated molecules leading to a more uniform layer over the chip.

3.3. Electron Beam Lithography (EBL) and resist development

Electron beam lithography (EBL) is a technique needed to transfer a pattern onto a chip where an electron sensitive resist had been previously deposited. The Raith Voyager EBL System is employed. The beam acceleration is 50 kV which is a high value necessary to limit scattering processes, while beam current is I= 0.33 nA. The exposure dose ranged between 175 and 215 μC/cm^2.
It is interesting to have some insight on the working procedure of the EBL and on its accuracy. As mentioned before the machine allows for a resolution around tens of nanometers which makes it possible to fabricate nanometric featured devices. EBL is a raster-scanning tool for pattern generation which enables for high resolution but long writing times. The whole design is internally divided into writing fields which are independently scanned. As a consequence a major problem is the stitching error, which can arise when the last exposed pixel of a field and the first one of the adjacent and subsequent one do not overlap sufficiently to implement the correct pattern [16].

3.4. Reactive Ion Etching

Reactive ion etching (RIE), performed with Oxford Plasmalab 100 shown in Fig.3.6, is a dry etching technique exploiting plasma to remove the superconducting material. Excited molecules like CF_4 are very reactive, and ionic species like CF_3+ are accelerated by the RF field conveying energy to the surface. Plasma etching is a combination of chemical (reactive) and physical (bombardment) processes. Two inlets at the top of a vacuum chamber are present which injects gaseous reactive species, usually CF_4 or O_2 for the case of NbTiN etching [16]. The chip is placed on a wafer holder which enters automatically the chamber. RIE etching has multiple adjustable parameters, such as gas flow, discharge power, chamber pressure, and density as well as distribution of etching pattern. In this thesis just etching time was taken into consideration. Since to fabricate a 9 nm Niobium Titanium Nitride (NbTiN) an etching time of 25 s is usually considered [17] and assuming a constant etching time, to produce a 12 nm Niobium Titanium Nitride (NbTiN) an etching time of 35 seconds is employed.

Figure 3.6: Oxford Plasmalab 100 for RIE etching

4 | Fundamental aspects of superconductivity

Theory	Restriction	Physics described
London model	$\lambda > \xi$ constant λ, ξ $(T \ll T_c)$	Electromagnetism
Macroscopic quantum model	$\lambda > \xi$ constant λ, ξ $(T \ll T_c)$	Electromagnetism Quantum behavior
Modified London model	$\lambda > \xi$ constant λ, ξ $(T \ll T_c)$	Electromagnetism Quantum behavior
Ginzburg-Landau theory	$T \approx T_c$	Electromagnetism Quantum behavior Phase transition
BCS theory	Classic superconductors	All essential physics Microscopic behavior

Figure 4.1: Summary of theories of superconductivity[18]

In this section the physical properties of superconductor devices are given to grasp the behavior of such devices in the superconducting regime. Moreover, these are needed to

understand the reasons behind the developments of theoretical models. Many theories exist dealing with superconductivity as shown in Fig.4.1. In this project, we will only discuss two of them: the London model and the Bardeen-Cooper-Schrieffer one. This is done because the London model allows to describe the behavior of superconductor properties recurring to relatively easy equations, while BCS theory is necessary if we want to understand the microscopic mechanisms which take place in superconducting materials. The latter one is also needed to derive useful parameters which cannot be derived with phenomenological theories.

4.1. Experimental evidence

To better understand the working principles of superconducting nanowire single photon detectors it is necessary to recall the most relevant aspects associated with the theory of superconductivity. Superconductors exhibit application-relevant characteristics such as zero resistivity, resulting in no power dissipation and perfect diamagnetic behavior (Meissner effect). Both these characteristics appear once the superconductor material temperature becomes smaller than its critical temperature Tc. The critical temperature Tc of a superconducting material is the value for which the material experiences a phase transition from the normal conducting state into the superconducting state [18]. The presence of a phase transition occurring at Tc is suggested by the abrupt change of the specific heat (Fig.4.2). This behavior in the specific heat is interpreted as a reconfiguration of the electronic state of the material. Superconductivity can be destroyed not only if

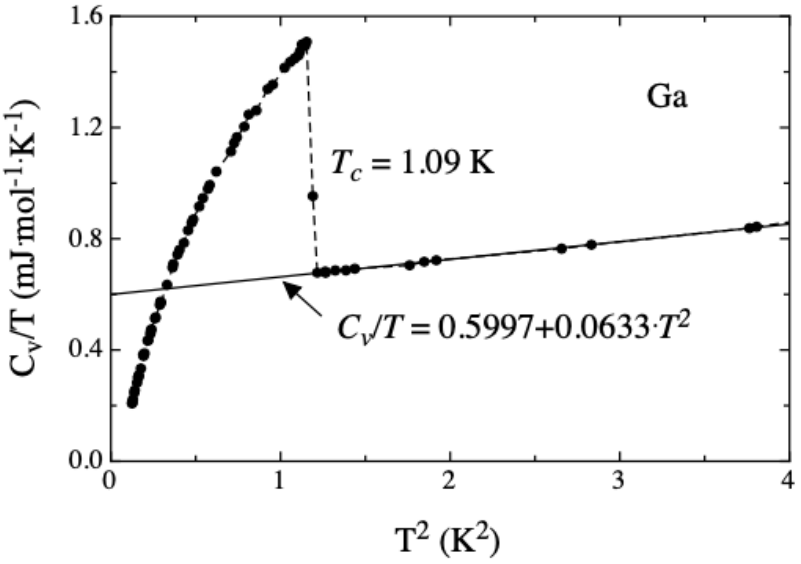

Figure 4.2: Specific heat behavior of a superconductor material[18]

the critical temperature is overcome but in two other additional cases: 1-a current flows through the device with a value larger than a threshold one (critical current value Ic), 2-a magnetic field is applied with a value larger than a threshold one (critical magnetic field Hc). Both these values are specific for each superconductive material. The critical magnetic field Hc=Hc(T), which is a function of the temperature, allows to make a further distinction between superconductors, namely type I and type II materials. In the first case (type I), only two domains in the graphic relating the critical magnetic field and the temperature are present, the superconducting (Meissner) state and the normal state. In

the second case there is an additional one, in between the Meissner one and the normal one, called "vortex" state. If the superconductor is in this region it will be populated by normal-conducting region of vortex shape. The graph showing the different behavior of the critical magnetic field as a function of the temperature is reported in Fig.4.3

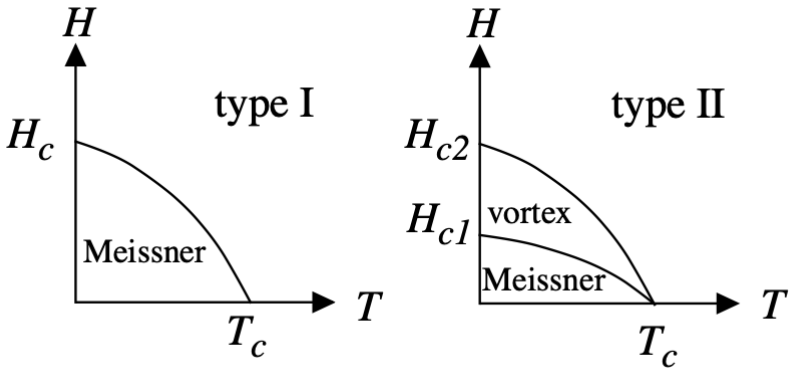

Figure 4.3: (a-left) type I (b-right) type II[18]

4.2. Superconducting materials

The periodic table depicted in Fig.4.4 shows that superconductivity is not rare in materials below their critical temperature. Nevertheless, for some of them it is necessary to reach not only very low temperature but large pressure values as well.

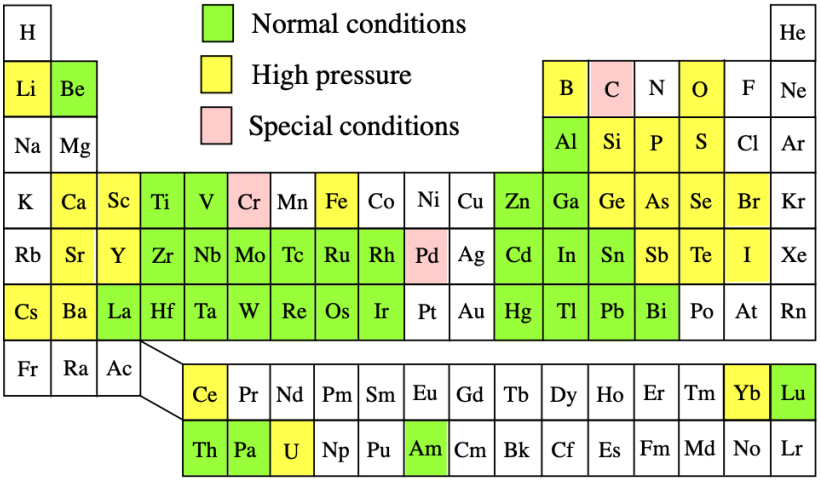

Figure 4.4: Superconducting materials[18]

As stated in the introduction, the main limitation in superconductors application is the

very low working temperature. Much effort has been placed in the research of high critical temperature superconductors, as this feature will allow easier operating conditions. For this reason it is interesting to report the highest value for Tc that some compounds show in Fig4.5 [18].

Material	Abbreviation	T_c (K)	Year
$La_{1.85}Sr_{0.15}CuO_4$	LSCO	39	1986
$YBa_2Cu_3O_7$	YBCO	92	1987
$Bi_2Sr_2Ca_2Cu_3O_{10}$	BSCCO	110	1988
$Tl_2Ba_2Ca_2Cu_3O_{10}$	TBCCO	125	1988
$HgBa_2Ca_2Cu_3O_8$	HBCCO	135	1993

Figure 4.5: Critical temperature values[18]

4.3. Modified London theory

The London equations are a phenomenological derivation of Maxwell's ones. Indeed, Maxwell equations are modified to reproduce the empirical properties of the superconducting materials. Both type I superconductors and type II superconductors in the Meissner state below Hc1 can be described by the two London equations: the first one is is linked with zero resistivity behavior (perfect conductor) while the second one reproduces the Meissner effect (screening of an externally applied magnetic field). It is important to highlight that the second London equation is a particular case of the first London equation. Indeed, in the analytical derivation of such formulas, which can be found in[18], the second London equation requires a null integration constant. This result cannot be inferred just from considering the zero resistivity behavior. As both of them are derived starting from (different) phenomenological considerations, it is clear that two properties exhibited by these materials don't have the same relevance. Indeed, the interpretation is that the second London equation is a more fundamental equation describing superconductivity and thus the Meissner effect is a more fundamental property for superconductivity than the vanishing resistivity[18]. Here, the two equations are reported:

$$1. \quad \mathbf{E} = \frac{\partial}{\partial t}(\Lambda J) \tag{4.1}$$

$$2. \quad \lambda^2 \nabla \times \nabla \times \mathbf{B} + \mathbf{B} = 0 \tag{4.2}$$

where, $\Lambda = \frac{m}{nq^2}$ and, as the charge carriers are Cooper pairs, the following relations hold $m = 2me$, charge $q = 2e$ and density $n = 1/2ne$. λ, appearing in the second London equation, gives a measure of how far an applied magnetic field penetrates into the superconductor and is a further discriminant between type I and type II superconductors.
However, in order to be able to describe type II superconductors in the vortex state it is necessary to recall the modified version of the second London equation. Vortex formations within a type II superconductors are experimentally observed. A possible way to examine this is by performing a scanning tunneling microscopy (STM) between a normal conducting tip and and a type II superconductor surface, separated by a very small gap, and then analyze the current versus applied voltage characteristic. As vortices are normal conducting regions the tunneling will either be i) between a normal conducting tip and a normal conducting vortex core (N–I–N tunneling) or ii) between a normal conducting tip and a superconductor (N–I–S tunneling). The two different I-V characteristics are reported in Fig.4.6. The linear one refers to normal conducting regions of the surface(vortices) which exhibit a resistive slope, while the gap represents the superconductive one.

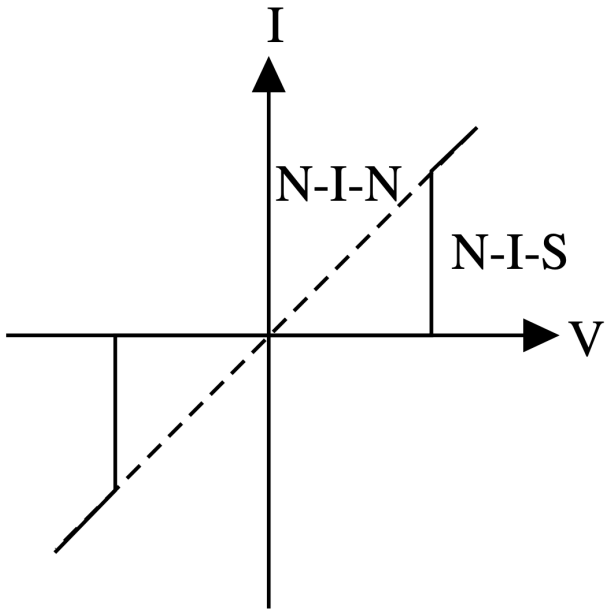

Figure 4.6: Scanning tunneling microscopy I-V characteristic in a type II superconductor[19]

The vortex is modeled as a cylindrical region of normal conducting material which is encircled by a supercurrent, responsible for the screening of the magnetic flux from the rest of the superconductor [19]. These formations arise to minimize the overall energy of

the material as it can be inferred from the Ginzburg-Landau theory. The coherence length ξ represents the core size of the vortex, while the penetration depth λ is the characteristic distance for which the field decays from both the vortex core and from the superconductor surface towards the inner part of the material. It is verified that $\lambda > \xi$ for type II and $\lambda < \xi$ for type I superconductors. A simple argument to understand such condition could be that if the penetration depth of a superconductor is much smaller than the vortex core, there would be no energy gain coming from destruction of superconductivity as the volume of the vortex is larger than the volume for which the magnetic field is allowed within the material.
To correctly describe a type II superconductor in the vortex state also the magnetic field passing through the vortices must be taken into account. It can be demonstrated that just an infinitesimal magnetic flux is allowed within the vortex, identical to the flux quantum $\Phi_0 = \frac{h}{2e}$. The modified London equation further contemplates such contribution:

$$\lambda^2 \nabla \times \nabla \times \mathbf{B} + \mathbf{B} = \mathbf{V(r)} \tag{4.3}$$

where, V($\mathbf{r}$) is the vorticity, i.e., the overall magnetic contribution of vortices within the material.

4.4. BCS microscopic insight

The London theory is capable of describing the superconducting behavior of type II superconductors with relatively simple equations. Indeed, such theory is more suitable whenever dealing with applications concerning superconductivity. Nevertheless, some parameters and ideas which are used in the following, can only be understood referring to the Bardeen-Cooper-Schrieffer (BCS) theory. When dealing with the conduction electrons of metals or metal alloys the free electron gas model is commonly used. Such electrons, obeying the Pauli exclusion principle, can occupy just one energy level and thus can be fully described by a unique combination of quantum numbers (spin included). The density of states[20] as a function of the electron energy is given by:

$$D(E) = \frac{V}{2\pi^2}\left(\frac{2m}{\hbar^2}\right)^{3/2}\sqrt{E} \tag{4.4}$$

Therefore, the conduction electrons will gradually occupy available states of increasing energy and at T=0, up to a maximum level Ef , the Fermi energy level which is usually around some eV. At vanishing temperature, there is a clear distinction between occupied levels and unoccupied ones, as no thermal excitation can be induced into the system. As

all the lowest energy levels are occupied, how can we justify a further reduction in energy taking place at Tc? It must be concluded that such decrease must derive from an attractive interaction involving electrons (abandoning a single electron picture). Electrons in a metal can interact through the exchange of a phonon (lattice vibration quasi-particle). When an electron scatters with the lattice from a state **k1** to **k2**+**q** creates a phonon carrying a crystal momentum -**q**. After that, another electron can also scatter with the lattice, thus acquiring such phonon. In this phonon-mediated process, usually referred to as "pairing mechanism", it can be demonstrated that a pair of electrons can have an energy smaller than the sum of the individual energies. Such pairs are the so called Cooper pairs and are responsible for the thermodynamic phase transition occurring at Tc. In this scenario an energy gap appears close to the Fermi level. A schematic of the gap is reported in Fig.4.7. The energy gap is proportional to the critical temperature through

$$\frac{2\Delta(0)}{K_b T_c} = 3.53, \tag{4.5}$$

where $\Delta(0)$ is the half the energy gap, k_B the Boltzmann constant and T_c the critical temperature [20]. The phase transition, as a consequence of Cooper pairs generation, imply that electrons within the range ($[E_F - \Delta(0), E_F]$) decrease their energy. Therefore, the density of states in the superconducting regime $D_s(\xi)$ is larger with respect to the normal state.

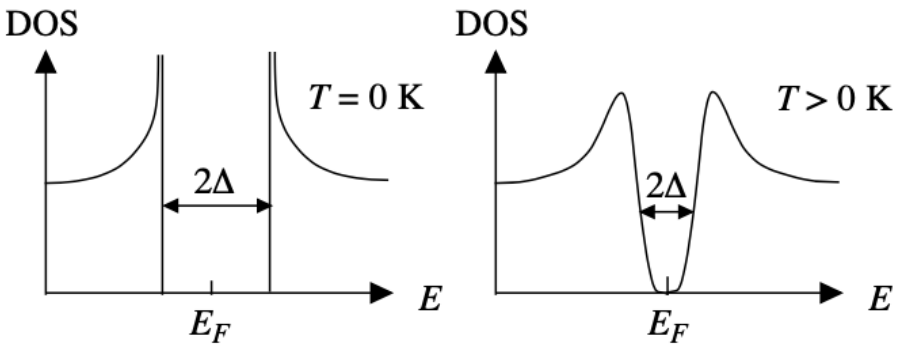

Figure 4.7: Superconducting gap (a) at T=0 (b) T>0 [20]

5 | Superconducting nanowire single photon detectors (SNSPDs)

5.1. Detection mechanism (direct)

The process concerning the detection mechanism is schematically reported in Fig.5.1. The detection process is initiated by a photon impinging on the superconducting device (I) with energy E=hν where, h is the planck constant and ν is the frequency, which, loosing energy, increases locally the temperature of the device to a larger value than bath temperature and Tc, the critical temperature of the superconductor. Upon phonon dissipation, a normal state region is created, referred to as hot-spot (II), which grows up to a maximum dimension (III) and subsequently decays(IV). The bias current, flowing through the device, experiences a normal-conducting domain, resulting in a detectable signal if one of the following conditions are met: either the hot-spot covers the whole cross-sectional area of the device (as schematically shown in the picture (III)), or the current, which is forced to a narrower cross-section, overcomes the critical one. Indeed, if the same current is restricted to flow into a smaller area the current density must increase.

$$I = const = I_b \tag{5.1}$$

$$I = Jwt \rightarrow J = \frac{I}{wt} \tag{5.2}$$

As a consequence of the Ohm law and the creation of a normal domain region, an electrical signal is generated detectable with a suitable read-out circuit [21]. Superconductivity is then recovered as the thermal diffusion allows for the operating conditions to be restored. As the hot-spots are usually very small (a brief discussion on hot-spot dimension is given in the following), a significant bias current I_b, close to the critical one I_c of the superconducting structure is needed. If we assume a cylindrical hotspot, centered around

the interaction point, the following threshold condition for the current is required[21]:

$$I >= I_{th} = I_c(1 - 2\frac{r_0}{w}), \tag{5.3}$$

where, I_c is the critical current, r_0 the maximum radius of the hot-spot and w the width of the nanowire.

$$r_0 = \sqrt{\frac{\Delta E}{\pi d \Delta H}}, \tag{5.4}$$

where ΔE is the excess delivered energy, d is the film thickness and ΔH represents the enthalpy difference per unit volume between bath temperature and the critical one of the device.

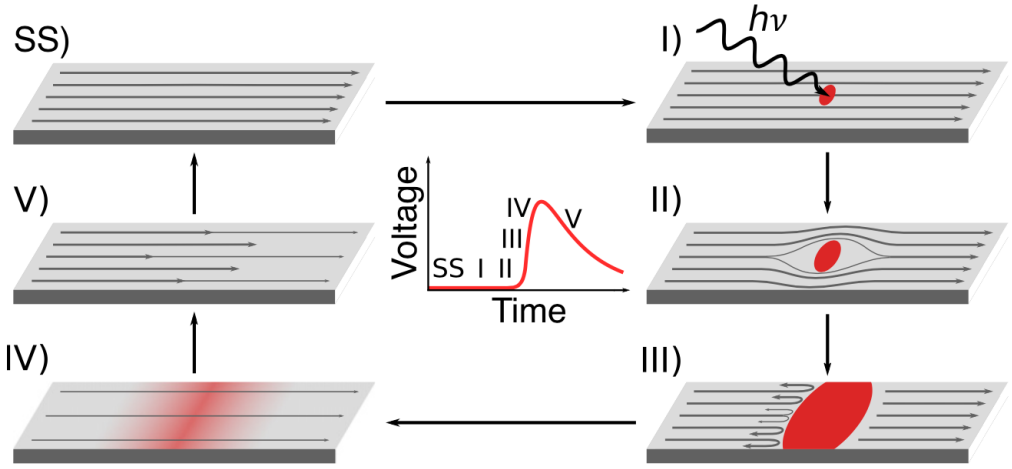

Figure 5.1: I) photon impingement onto the superconductor device II)hot-spot creation III) hot-spot diffusion covering the whole cross-sectional area IV) decaying of the hot-spot formation V) increase of the bias current flow SS) restored superconducting parameters [7]

With this in mind, it is possible to understand the reason why for such devices large bias currents are needed to reach near-unity detection efficiency. An example of detection efficiency as a function of the bias current is the one in Fig.5.2 where a plateau is present[14]. In this picture the count rate as a function of bias current is reported for different substrate. The saturation (plateau) is reached for relevant fractions of the bias current.

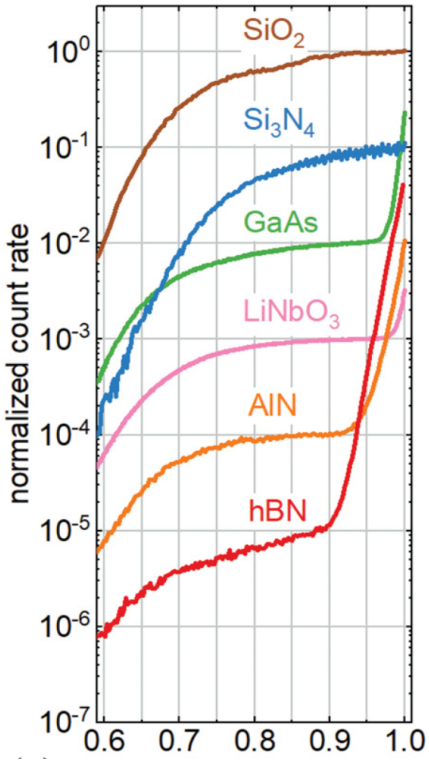

Figure 5.2: NbTiN count rate (efficiency) as a function of the normalized bias current[14]

5.2. Hot-spot dimensions

The hot-spot dimension is a crucial discussion for detection purposes. Starting from an intuitive discussion we can argue that, since the energy carried by a photon is $E = h\nu$ and so $E = \frac{hc}{\lambda}$, the larger the wavelength of the impinging photon the smaller the hot-spot size will be, since less energy associated with the photon will turn into thermal one and will be delivered to the film. Recalling the discussion of the previous section about the hot-spot cylindrical model, the following equation, for the hot-spot minimum size to be detected, is derived[22]:

$$D > w(1 - \frac{I}{I_c}), \tag{5.5}$$

This equation only considers that the ratio of the induced normal region diameter (assumed as cylindrical) and the width of the nanowire. Indeed, in this simplified model it is considered that the hotspot diameter is usually greater than the thickness of the nanowire and thus just the lateral dimension is taken into account. With this in mind, it is necessary to estimate the width for which IR light at $\lambda = 850$ nm does not induce a sufficient variation in the cross-sectional area to increase the current density to a value larger than the critical one. This is done in order to not detect (suppress) the scintillation events, resulting in indirect detection event, coming from the substrates and to successively esti-

mate the device direct absorption of X-rays [2]. As the scintillation is in the visible and IR regime (see SiO_2 scintillation section), 850 nm represents a good enough threshold. Indeed, if it is made sure that these photons are not detected, all impinging photons with larger wavelength will not be detected with sufficient efficiency. An additional condition is that these indirect IR light induced counts must be suppressed for any bias current lower than the critical one, as in operating system the current flowing through the device can be extremely close to it. Let's fix the bias current to a value $I_b = 0.9I_c$ and the wavelength of the incoming light to $\lambda = 850$ nm. The estimation of the hot-spot dimension at that given wavelength is derived from [22] and the relevant figure is here reported. It is clear

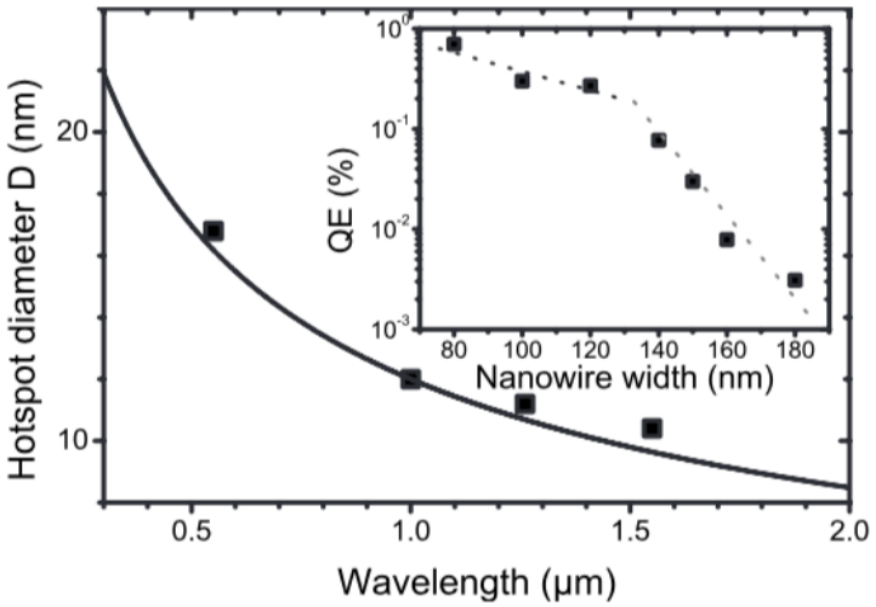

Figure 5.3: Hotspot diameter as a function of the wavelength for NbN[22]

from Fig.5.3 that a $\lambda = 850$ nm produces an hotspot of about diameter $D = 12.5$ nm. Assuming the cylindrical area of the hotspot it is possible to derive if the reduction in the cross section induces a current density to a value larger than the critical one. This is done for the dimensions that are taken into account in this project, so for $t = 12$ nm and $w = [0, 07/0, 1/0.15/0.2]$ μm. Following the calculations in the left column of the table in Fig.5.4 the current flowing through the device upon absorption of a photon is obtained (value with respect to the critical one). This simple estimation allows us to conclude that the width threshold dimension for which IR counts are suppressed falls within the selected range (ideally for this model if the j2 value is larger than unity the detection takes place). A final remark before concluding this section must be done referring to Fig.5.3. In reality, the previous model, which has been used to find an approximate range of widths

width (um)	0.07	0.1	0.15	0.2
thickness (um)	0.012	0.012	0.012	0.012
A1(um^2)	0.00084	0.0012	0.0018	0.0024
hot-spot dimension (um^2)	1.23E-04	1.23E-04	1.23E-04	1.23E-04
A2 (um^2)	7.17E-04	1.08E-03	1.68E-03	2.28E-03
J2=0.9*J_c*(A1/A2) in Jc	1.05E+00	1.00E+00	9.66E-01	9.48E-01

Figure 5.4: Density current induced upon photon impingement of $\lambda = 850$ nm

for experimental purposes is not completely accurate. Indeed, assuming a constant current I right after a photon impingement onto the device is a rough estimation since, as discussed in the section concerning the detection mechanism, the resistance of the hot-spot is considerably greater than the one in parallel in the read-out circuit. This implies that the actual current flowing in the remaining cross-sectional area is smaller and thus this model overestimate the width of the nanowire. Indeed, if the current I is smaller, a smaller width would be needed induce the detection process. Although for this discussion NbN has been used, we can infer that similar results would be obtained by employing NbTiN as the two compounds show similar properties [23]. Another consideration is that the threshold represented by equation $w\sqrt{\lambda} < K_1$[22], which is analogous to the one we derived, will result in a drop of DE (Detection Efficiency) and not on a proper threshold between detected and suppressed photons. Analogous results are obtained if, instead of varying the width, the bias current or the energy of photons are changed. Indeed, in both cases a threshold value where detection efficiency drops can be found.

5.3. NbTiN

Niobium titanium nitride (NbTiN) is used as superconductive thin film because of its excellent time resolution, high efficiency (over 90 %), low time jitter of 10 ps with, a count rate of hundreds of MHz and an operating temperature around 2K. Other amorphous materials as WSi are restricted to sub-Kelvin temperatures which cannot be reached with the cryostat present in the laboratory. Nevertheless, NbTiN fabrication procedure is challenging because of its crystalline structure. As some of the properties are substrate dependent it is reasonable to first state the reason for the choice of such substrate (SiO_2) and then provide the main properties. SiO_2 is generally employed for fiber-coupled devices due to the refractive index difference with respect to the underneath silicon which gives rise to a weak optical cavity[24]. In [14] it is reported that NbTiN on SiO_2 substrate present a sheet resistance Rs=339 $\frac{\Omega}{\square}$ a root mean square surface roughness Rq=0.4 nm

and a critical temperature Tc=10.2 K. The low value of Rq which is possible for few substrates has implications on the detected dark counts: indeed it was reported that lower values of Rq correlate with a low number of dark counts[14]. On the contrary, other properties are more independent on the substrate as for the kinetic inductance, which is indirectly obtained from the pulse exponential decay time constant as it is shown in the next section. The count rate characteristic was previously shown in Fig.5.2. When dealing with superconductors a fundamental quantity is represented by their superconductive gap. Indeed, the number of quasi-particles generated by the absorption of a photon can be estimated as[25]

$$N_{quasi-particles} \approx \frac{E_{photon}}{1.74\Delta} \tag{5.6}$$

where E_{photon} is the photon energy and Δ is the superconducting gap energy. From the previous equation it can be inferred that the lower the energy gap the more sensitive the material is to infrared (IR) light. For our purpose we do not want this value to be too low. NbTiN shows a superconducting energy gap $2\Delta(0) = 36.5\text{cm}^{-1}$ with $2\Delta(0)/k_BTc = 3.72$[26]. The minimum binding energy of a Cooper-pair is $2\Delta(T)$. When $T << Tc$, as in our case, we can approximate $\Delta(T) \approx \Delta(0)$ which, from the previous formula delivers an energy gap of 3.26 meV. As the scintillation energy of SiO_2 is around $E = 2.9$ eV a single incoming photon can in theory break ≈ 900 Cooper-pairs[27]. Such value is indeed quite large and thus NbTiN is rather sensitive to infrared (IR) light. Almost all the parameters reported so far are thickness dependent, thus we expect different values for such quantities as the employed thickness is different from the one in[14]. Nevertheless, these will be used as reference parameters for our considerations.

5.4. Quartz scintillation

As previously stated in [2] the main contribution for NbTiN indirect detection mechanism comes from its SiO_2 substrate. In particular, many processes such as lower-energy X-ray photons, optical photons, hot electrons, and phonons can in principle be responsible for the indirect detection events. Nevertheless, at least three arguments suggest that the substrate luminescence might be the major contribution. First SiO_2 X-ray induced scintillation falls within the "blue" range, approximately around a wavelength of $\lambda = 425 - 440nm$. Secondly, SiO_2 is transparent to such wavelength, enhancing the possibility for those photons to reach the superconductor detector [28].

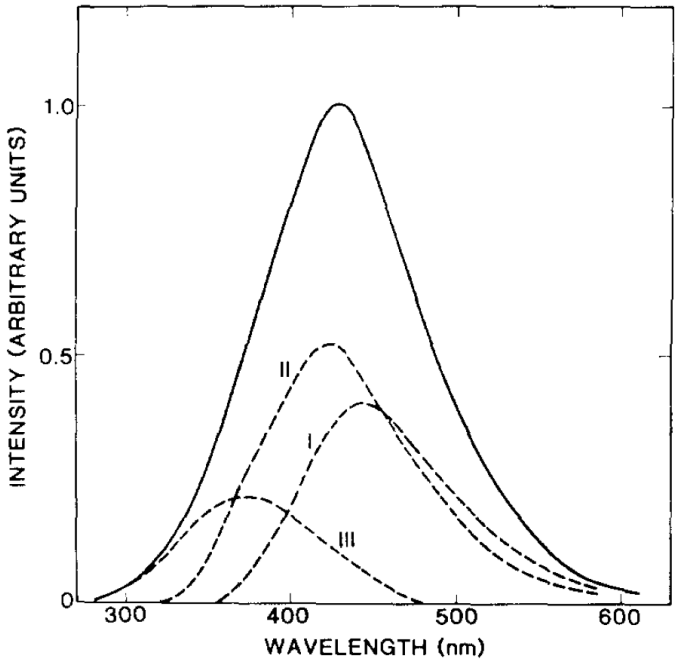

Figure 5.5: SiO2 X-ray induced luminescence [28]

Third, in [2] a nanowire with sufficiently small cross-sectional area for SiO_2 luminescence direct detection is present, considering previous calculation on hot-spot dimension. SiO_2 luminescence is mainly composed of three bands and that are reported in Fig.5.5

For our experimental results, a light source with $\lambda = 850$ nm (the smaller wavelength relevant for the objective of this thesis) has been used. One might say that the suppression of counts coming from the scintillation of the substrate centered at $\lambda = 425-440$ nm could imply different dimensions from the one that has been used. Let's compute the same table as 5.6 for $\lambda = 425-440$ nm. It is possible to verify that at least 0.2 μm width satisfies the suppression requirement. It is reminded that this is a limiting case, i.e. an overestimation is done concerning the actual dimension of the wire. Furthermore, no actual suppression takes place with this condition but a DE (detection efficiency) drop (ideally for this model if the j2 value is larger than 1 the detection takes place). Furthermore, photons will lose energy before reaching the superconducting device, shifting the overall spectrum towards longer wavelengths.

5.5. Indirect detection mechanisms

In this section the indirect detection mechanism is discussed. The expression indirect detection mechanism refers to detection events which are mediated by the substrate.

width (um)	0.07	0.1	0.15	0.2
thickness (um)	0.012	0.012	0.012	0.012
A1(um^2)	0.00084	0.0012	0.0018	0.0024
hot-spot dimension (um^2)	2.40E-04	2.40E-04	2.40E-04	2.40E-04
A2 (um^2)	6.00E-04	9.60E-04	1.56E-03	2.16E-03
J2=0.9*J_c*(A1/A2) in Jc	1.26E+00	1.13E+00	1.04E+00	1.00E+00

Figure 5.6: Density current (last row) expressed as a fraction of the critical current density. induced upon photon impingement of $\lambda = 450$ nm

Indeed, as the substrate can also absorb the incoming light, it is possible that secondary emitted particles or back-scattered photons are responsible for the previously described detection mechanism (direct) to take place. As a rule of thumb, the more energetic the incoming light the less relevant is the direct absorption of the thin nanowire and so the direct detection mechanism. For $\lambda = 850$ nm the energy $E = 1.46$ eV while for X-ray, as those used in [2], $E = 8$ keV. To estimate the mass photo-absorption coefficient in a NbTiN film NIST (National institute for standard technology) an online calculator is used. As it can be seen from Fig.5.7 a value of $1.517 * 10^2$ for the mass attenuation coefficient is found associated to an energy of 7.9 keV, close to the desired one. For $E = 1.46$ eV incoming energy, as the calculator is not available for this energy range, the Bragg-Pierce condition is used:

$$(\mu/\rho)_{1.46eV} \propto K\lambda_{1.46eV}^{2.5/3} Z^4, \tag{5.7}$$

Where the value of the wavelength is known. As value of the mass photo-absorption coefficient at $E = 8$ keV is known it is sufficient to take the ratio of the two Bragg-Pierce conditions (exponent for the wavelength = 2.5):

$$(\mu/\rho)_{8keV} \propto K\lambda_{8keV}^{2.5/3} Z^4 = 1.517323 * 10^2 cm^2/g, \tag{5.8}$$

$$(\mu/\rho)_{1.46eV} = (\mu/\rho)_{8keV}(\frac{\lambda_{1.46eV}}{\lambda_{8keV}})^{2.5/3} = 1.517323 * 10^2 * (\frac{850 * 10^{-9}}{1.55 * 10^{-10}})^{2.5/3} = 3.37 * 10^{11} cm^2/g, \tag{5.9}$$

Using for the density of the material $\rho = 6.1 g/cm^3$ the computed values correspond to an inverse of the linear attenuation coefficient of ($1/\mu$ is the distance in the material for which the intensity of the incoming beam is reduced of a factor 1/e):

$$1/\mu_{1.46eV} = 4.0 * 10^{-13} cm, \tag{5.10}$$

$$1/\mu_{8keV} = 1.08 * 10^{-3} cm = 1.08 * 10^{-5} m, \tag{5.11}$$

The Pierce-Bragg condition is suitable when the photoelectric effect is predominant and thus it cannot be applied to IR case. Nevertheless, it is an easy approach to state that a nanometric film is thick enough to absorb much of the incoming light. The relevant result is that within a length of $l = 10.8$ μm the X-ray are relevantly absorbed implying that as stated in [2] the main contribution for unity detection efficiency must be ascribable to substrate mediation.

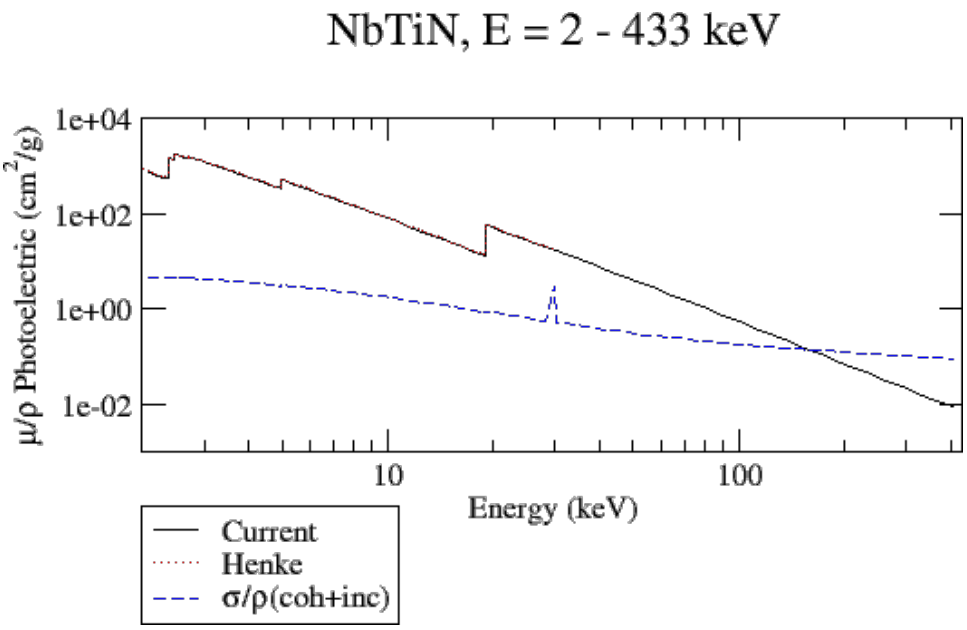

Figure 5.7: Mass attenuation coefficient for NbTiN

5.6. System detection efficiency

The overall efficiency for SNSPD photon detection is made up of three different contributions: η_{abs} which refers to the efficiency in the absorption event, the electronic efficiency η_e which is related to the probability that a photon which is absorbed produces a detectable electrical signal and η_{oc} which is associated to the losses introduced by the optical system, mainly referring to fiber coupling [29] (the latter one should not be taken into account for flood illuminated systems [17]).

$$\eta_{tot} = \eta_{oc}\eta_e\eta_{abs} \tag{5.12}$$

In particular η_{abs} is also coupled to η_p via an empirical expression:

$$\eta_p = \frac{\eta_0}{(1 + (kd)^n)^2} \tag{5.13}$$

where η_0 is the largest η_p at the plateau with a saturated response efficiency. The denominator of η_p decreases following a power law in n with the thickness d while and k is a superconductor parameter [29].

5.7. Kinetic inductance

The kinetic inductance L_k can be regarded as an inertial mass of mobile charges, which in the case of superconductors are Cooper pairs, arising whenever alternating electric fields are applied [30][31]. As it will be seen in the following, the large value that the kinetic inductance can assume in a nanowire represents the main contribution to the impedance, since the dc resistance is zero in a superconductor. Furthermore, this value scales with the length of the device and it is inversely proportional to the cross-sectional area of the nanowire, which is dramatically small. It is important to derive the dependence of the kinetic inductance on geometrical parameters because, as it will be better explained later on, this value must be contained within a range of values. Equating the total kinetic energy of the superconductor carriers (Cooper pairs) with an equivalent inductive energy:

$$n_s(lwt)mv^2 = \frac{1}{2}L_K I^2, \tag{5.14}$$

where I is the super-current in the nanowire, n_s is the density of Cooper pairs, lwt is the volume of the conductor (length $\times$ width $\times$ thickness), 2m is the mass of a Cooper pair, and v is the average velocity of the Cooper pairs. Bringing all the terms to the left hand side of the equation and subsequently substituting the values from the Ginzburg-Landau

theory [20] [31]:

$$L_K = \frac{m}{2n_s e^2}\frac{l}{wt}, \tag{5.15}$$

This very simple equation imply that in nano-metric thick and wide devices, as those under investigation, the value for the kinetic inductance can be very large, ranging between 415 nH and 6.10 nH for NbN films of thickness 3-5 nm, widths around 20–400 nm and lengths ranging from 0.5 to 500 μm. Finally we report the formula of the kinetic inductance dependent on the superconducting gap:

$$L_K = \frac{lR_{sq}h}{w2\pi^2\Delta tanh(\frac{\Delta}{2K_bT})}, \tag{5.16}$$

An intuitive way to confirm that the major contribution to impedance is due to the kinetic inductance, determining the current recovery time and thus the maximum counts rate was done by [32]. Indeed, as both the room temperature resistance and the kinetic inductance are proportional in analogous way to the geometry of the device:

$$R_{300K} = \rho_{300K}\int\frac{ds}{A(s)}, \tag{5.17}$$

$$L_{300K} = l_{300K}\int\frac{ds}{A(s)}, \tag{5.18}$$

a linear dependence of the two quantities represents a proof of the previous statement [32].

It is relevant for our purpose to understand how the kinetic inductance L_k can be measured. A phenomenological model is proposed in [32], where $R = 50\Omega$ is the output parallel resistance, $R(t)$ is the time dependant resistance of the superconductor and L_K is the kinetic inductance of the nanowire (see Figure5.8). The presence of a normal-conducting regime (resistance Rn in parallel to the switch), upon hot-spot generation, corresponds to a switch opening (short circuit equivalent to superconducting state) as a fraction of the bias current is now forced to go through a resistive path. Indeed, while the switch is closed the bias current is utterly directed to the superconducting device, whereas if the switch is open it is necessary to consider the parallel between the generated resistance and the output one. The initial current I_b which flows in the superconducting device starts to decay with a time constant $\tau_{fall} = L_K/[50\Omega + R_n]$ to a final value $I_n = I_b\frac{50\Omega}{[50\Omega+R_n]}$ until the Joule dissipation power $i(t)R_n^2$ is enough reduced, and the superconducting regime is restored (and the switch closes). The current returns then to its original value with a time constant $\tau_{rise} = \frac{L_K}{[50\Omega]}$ and from the asymmetry of a generic pulse, as the one reported in Fig. 5.9, it results that $\tau_{rise} >> \tau_{fall}$ and it is therefore possible to conclude that

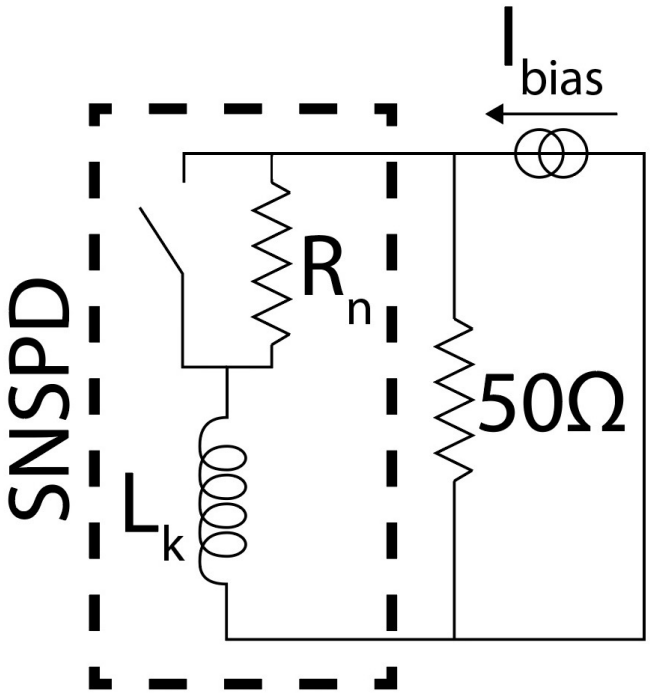

Figure 5.8: Device scheme

$R_n >> 50\Omega$. In the following the inverse formula relating the kinetic inductance to τ_{rise} will be used to derive the value of the kinetic inductance in the fabricated device

5.8. Latching mechanism

It has been discussed in previous sections that a short enough kinetic inductance is necessary to allow for fast detection, as $\tau_{rise} = \frac{L_K}{50\Omega}$ which determines the recovery of the superconducting state, is directly proportional to it. In this section, the latching mechanism is reported, which introduces a limit for the kinetic inductance towards small values. The result is that the value for the kinetic inductance is the result of a trade-off between fast detection and correct functioning of the device. As discussed in previous paragraphs, upon impinging of a photon onto the device the nucleation of a normal conducting domain results in a resistance Rn(t). The subsequent expansion of such domain due to heating dissipation is counteracted by negative electrothermal feedback from the load resistance. Indeed, the load resistance R_L in a parallel configuration with the one of the device, as depicted in the previous figure5.8 being much smaller than Rn(t), when the hot-spot reaches the maximum dimension (has demonstrated in previous paragraphs), diverts the

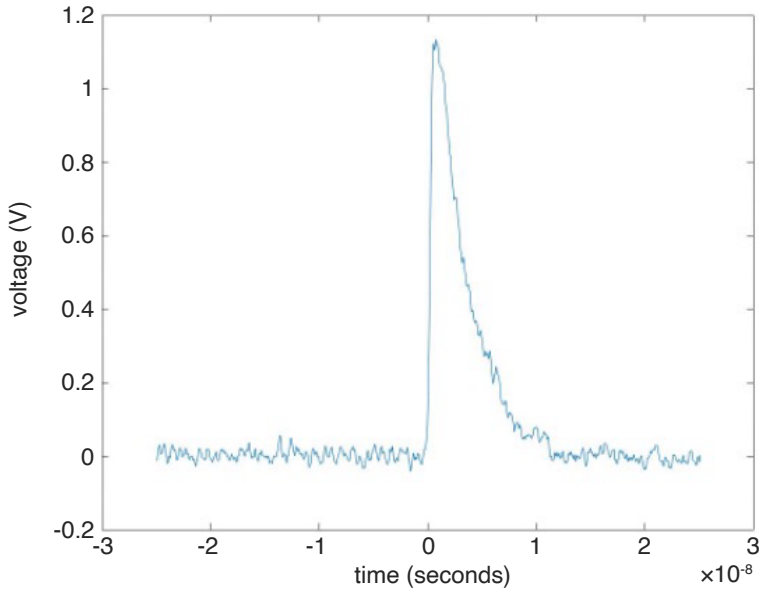

Figure 5.9: Pulse detected from oscilloscope which decays with a time constant τ_{rise}

current from the device path to the load resistance path. Such decrease, allows the system to reduce heat dissipation and restore the superconducting state. Nevertheless, if L is too short the feedback is stable: I_L, the current flowing through the load path, is sufficiently increased (before on the other wire the superconducting state is restored) to create an equilibrium configuration (latching) in both wire and thus leading to a stable and locked resistive domain, known as a self-heating hotspot [33]. For this reason, the desired working mode is the one where the electro-thermal feedback is unstable, allowing for self-recovering of the superconducting state.

6 | Reference article results

The aim of this work is to proceed in the evaluation of the indirect detection contribution upon X-ray illumination of a NbTiN SNSPD. Such experiment is presented in [2] and the most significant results, which give us a more complete overview over this project topic, are discussed. In the article a NbTiN device is used of width w= 70 nm and thickness t=10 nm over a subtrate of layered SiO_2 and Nb_2O_5. A microfocus X-ray source (Phoenix xs 160 T) with Copper anode and an acceleration voltage of 30 kV was used. The energy of the X-ray photons exhibits two main peaks where the intensity is confined, at energy $E_1 = 8.05$ keV and energy $E_2 = 8.9$ keV. The experiment is carried out employing a Silicon drift detector (SDD) allowing to both measure the spectrum and the total number of X-ray photons arriving at the SNSPD. A meandering SNSPD device is used with 0.5 filling factor, shown in Fig.6.1. A first characterization of the sample is done by measuring

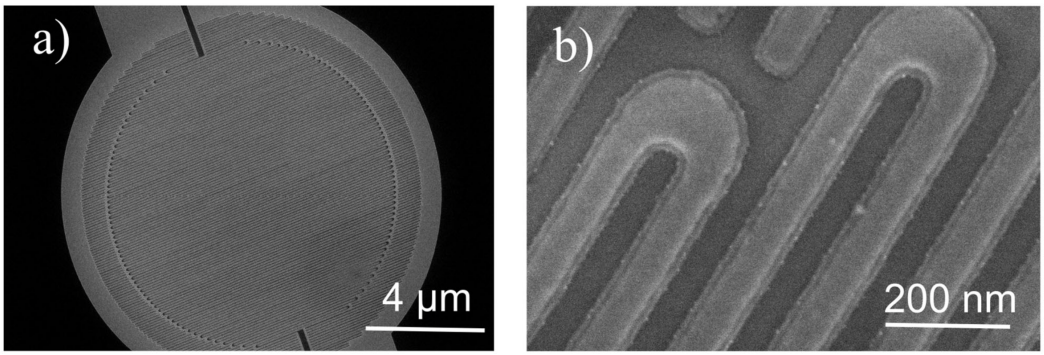

Figure 6.1: X-SNSPD from scanning electron microscope imaging[2]

the dark counts as a function of the bias current shown in Fig.6.2. The maximum value of dark count rate (DCR) is in the order of 10 kcps, a high value which can be attributed to fabrication imperfections. Indeed lower dark count rate values are usually achieved for shorter[34][14] and wider[35][36] nanowires.

Fig.6.2 clearly shows that the increase of the count rate in the region below 18 μA bias current is caused by the X-ray irradiation. Since the probability of absorption is very low, as it has been calculated in previous sections, the detection event must be triggered by secondary particles. In Fig.6.3 all sets of data show a linear behavior with an pro-

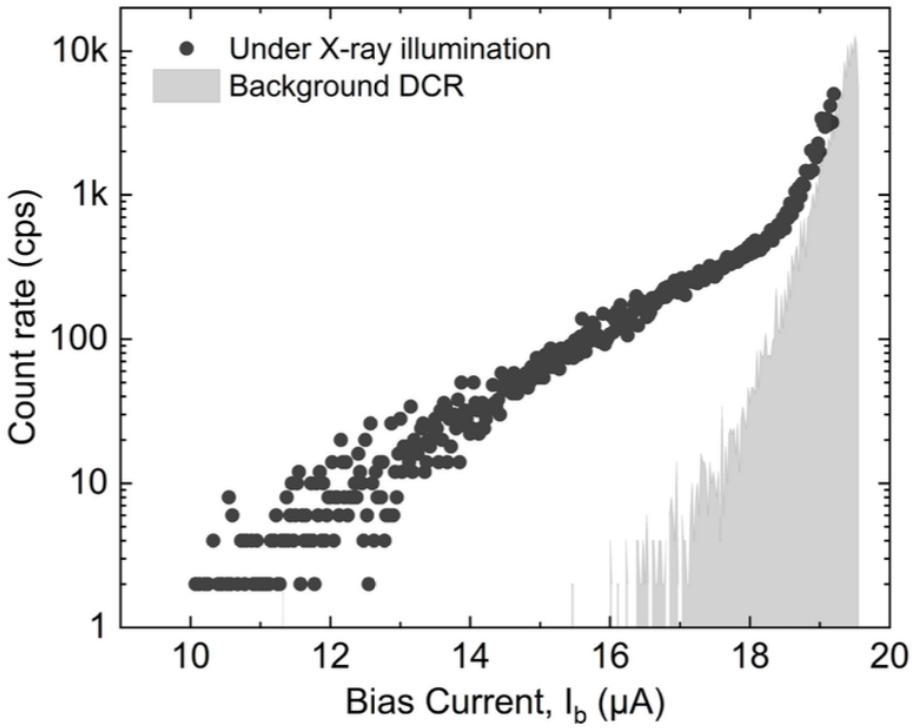

Figure 6.2: Count rate and dark count rate as a function of the bias current[2]

portionality factor increasing with the bias current. The slope values are i) 1.1, ii) 0.4, and iii) 1077 (see figure description). The last value is an additional proof of substrate detection enhancement: such a large value means that the role of the secondary particle is far more relevant than the direct absorption, exceeding it more than 1000 times. It is also argued that substrate mediation enhancement is not necessarily due only to substrate scintillation but also to hot electrons and phonons. However, it is recognized that the luminescence property of the substrate might be one of the main responsibles.

These results encourage further research around the substrate contribution for X-ray illuminated SNSPDs triggering also the idea of a substrate capable not only the of detecting the event but the energy too. In particular, the present work concentrates on fabricating a device which suppresses the SiO_2 scintillation, which is assumed the more relevant contribution in secondary particle emission responsible for the detection. An analogous experiment with different SNSPD widths, will allow us to understand how important is the contribution of the substrate scintillation. Indeed, if the reduction in detected events is consistent it will be possible to infer that SiO_2 scintillation is the main responsible and thus it will open the way to the application of SNSPDs with new substrates. In the opposite case, if no relevant reduction in detection events is recorded, it will be necessary to investigate other indirect mechanisms.

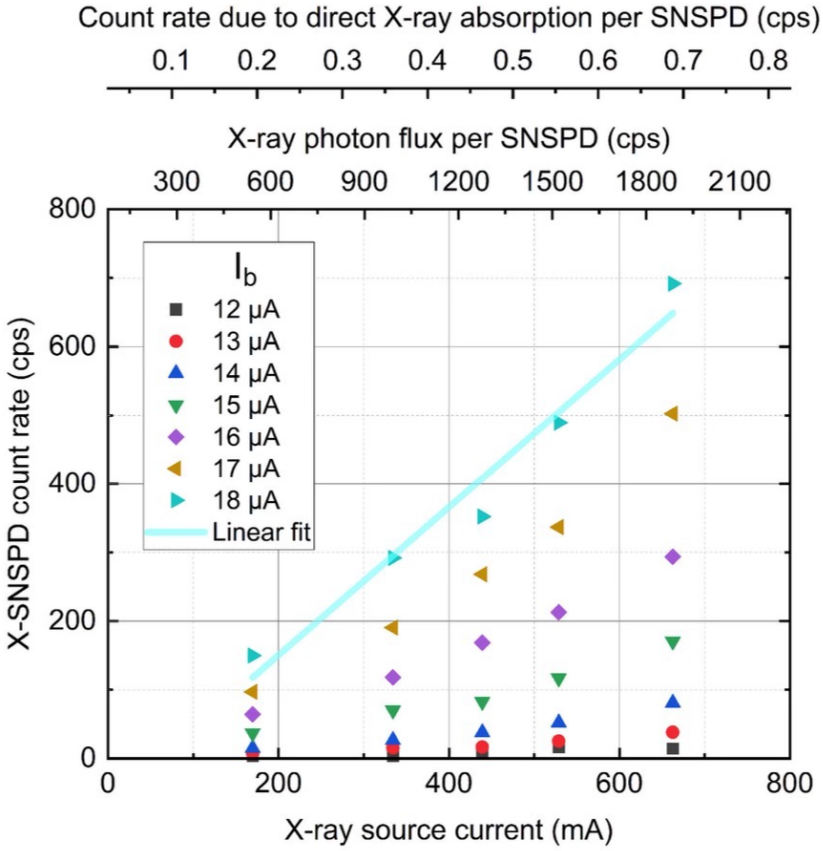

Figure 6.3: X-SNSPD count rate as a function of (i) X-ray source current, (ii) X-ray photon flux per SNSPD, iii) the count rate due to direct X-ray absorption[2]

7 | Measurement description and results

7.1. Measurement setup

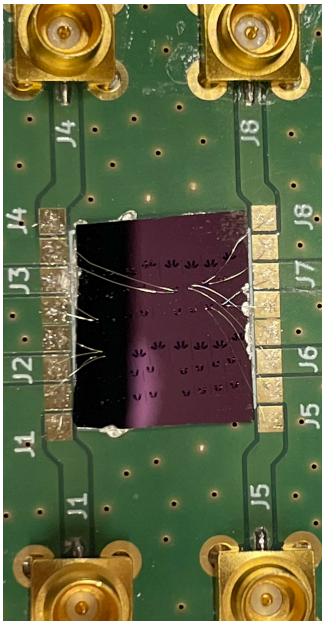

Figure 7.1: Al wire bonded SNSPDs onto a PCB

Figure 7.2: open PCB in cryostat with fiber end

To be able to perform the measurement, the fabricated chip is attached with silver glue on a grounded metal plane on top of a PCB (printed circuit board) suitable for the detection mechanism. It is then necessary to wire bond, with an aluminum wire, the PCB with the SNSPDs pads, the final squared ends of the device. A typical assembled SNSPD sample is shown in Fig.7.1. Fig.7.2 shows the PCB in the open cryostat. The wire connects the devices with the driver of the setup. Before loading the chip into the cryostat, it is possible to measure the room temperature device R_{RT} which as we have already seen

depends on the wire dimension through the following equation:

$$R_{300K} = \rho_{300K} \frac{l}{w * t}, \tag{7.1}$$

typical values are from a 0.1-2 $M\Omega$.

The experimental setup is schematically depicted in Fig.7.3. The vacuum pump and He compressor allow to satisfy the working condition of low temperature (with a nominal temperature T=3K) as well as low pressure ($5 * 10^{-5}$ mBar) to be obtained. A laser wavelength $\lambda = 850nm$ is connected through an optical fiber to a fiber terminal of the system. The electrical output is directed towards a driver (single quantum Eos) that amplifies, triggers, and reads-out detection events. The signal is then directed to a display screen and to an oscilloscope (LeCroy WaveRunner 640 Zi with 4 GHz bandwidth).
The output of the system allows to monitor the output voltage as a function of the bias current and the counts per second (they can be both dark count or signal counts depending on if the laser has been switched on). The oscilloscope is instead used to display the electrical signal waveform while performing the experiment. In addition to the time constant information of the pulse, which is associated to the kinetic inductance of the device, the oscilloscope is necessary as it signals whether the system is latching or not. Indeed, if the system latches, or equivalently, if the electro-thermal feedback of the system is stable, the waveform will appear as having a very long time constant (thus not recovering to superconductive state). If this is the case, lower bias current must be used for such devices to detect photons.

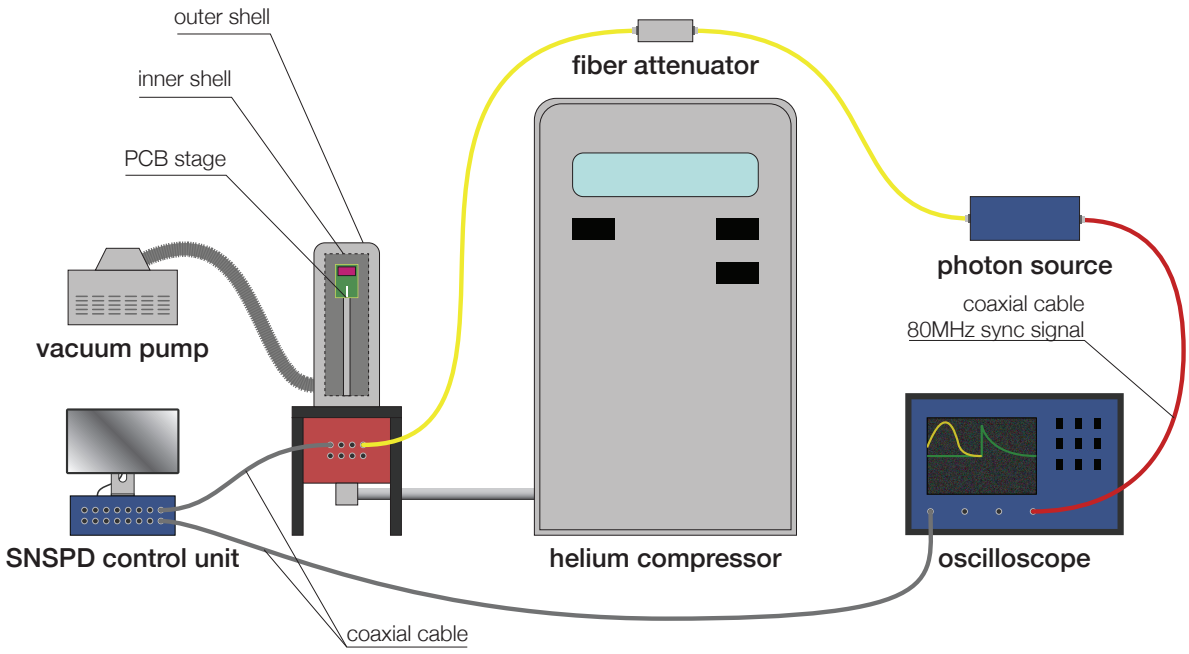

Figure 7.3: Measurement setup scheme

7.2. Device characterisation

As stated in previous sections, the fabrication of NbTiN superconducting nanowire single-photon detectors (SNSPDs) is rather challenging due to their crystalline structure. Therefore, it is important to characterise them with both a priori and a posteriori parameters, which compared to reference ones, will allow us to make a distinction between functioning and non-functioning devices. The parameters which are useful for this purpose are: room temperature resistance, critical current value, general behavior of the voltage characteristic as a function of the bias current and value of the kinetic inductance. In this section it will be discussed how to extract such parameters and what it can be inferred from out of range parameter values.

The room temperature resistance is the first parameter to be addressed. An ohmmeter is used where to extract the value of the room temperature resistance it is necessary to put in contact the positive and negative wires with the end pads of the SNSPD. Typical values are within the 0.1-2 MΩ window. If low values of the room temperature resistance are obtained, it can be inferred that during the fabrication process some resist was not properly removed in some regions within the hairpin, thus leaving the underneath superconducting layer. This will result in a short-circuit. On the contrary, large values of the

room temperature resistance are associated with narrower regions along the nanowire, usually referred to as "bottleneck regions". Saturated values (overload) are usually ascribed to the presence of material gaps in the device which prevent the current flow. The extracted values of the room temperature resistance of employed devices are reported in the tables in the result section.

The critical current value and the overall behavior of the voltage to bias characteristic represent additional criteria to evaluate correctly working devices. Fig.7.4 depicts the voltage to bias current behavior of SNSPD devices from the fourth experiment(n4) that was carried out (see result section). As Superconducting nanowire single photon detectors

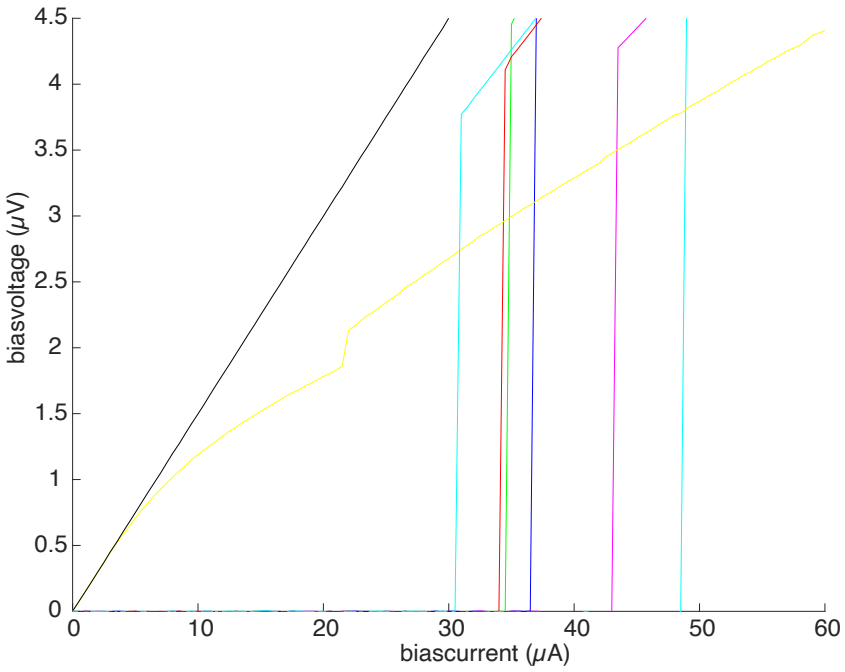

Figure 7.4: Voltage as a function of critical bias (experiment 4) (each color represent a different tested device, see relative table in the result section for comparison)

show no resistance if a current with lower value than the critical one is applied, the voltage over bias current characteristic is a flat function coincident with x-axis. Once the critical current value is reached, a voltage potential difference arises, exhibiting a linear characteristic whose slope depends on the load resistor (in our case 50Ω). However, different devices show different critical current values. The equation relating the critical current to the geometry of the nanowire is:

$$I_c = J_c w * t; \tag{7.2}$$

where J_c is the critical current density, w the width and t the thickness of the device. As both the thickness and Jc are kept constant, the critical current value should vary mainly because of the difference in width. The bias current application window is 0-66 μA. As it can be deducted from Fig.7.4 the black and yellow lines do not represent a superconducting characteristic. Indeed, both devices show a resistive behavior already from very low values of the bias current. The critical current value, instead, gives information about the status of the device if a comparison is made with critical current values of other devices. As previously stated, since the only varying parameter in the critical current equation (7.2) is the width, the characteristics appearing in Fig.7.4 should be associated, from left to right, with devices of increasing width. In addition, devices having the same widths should exhibit similar values for the critical current. With this in mind, a general consideration could be that critical current values lower than expected ones can be associated with narrower widths or with the presence of bottlenecks along the nanowire. Vice versa, larger Ic values are related to factual larger device widths. All these considerations are employed to discard not reliable devices or question the ones which are considered reliable. An example is reported in Fig.7.5 where the second cyan characteristic from the left refers to a w=150 nm device (J1 in experiment n3). Such device shows a relevantly lower value

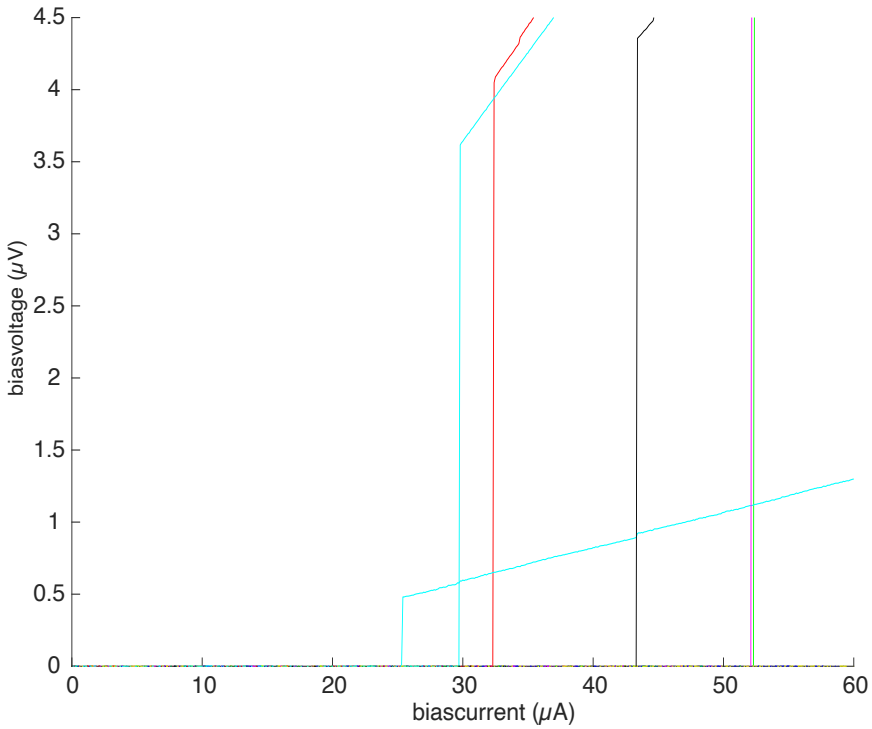

Figure 7.5: Voltage as a function of critical bias(experiment 3) (each color represent a different tested device, see relative table in the result section for comparison)

of the critical current, if compared to devices with analogous width (J5-green line and J8-purple line) and lower resistance value, if compared with an equivalent device (J8). This characteristics can arise from a combinations of both short-circuit, responsible for lower resistance, in some region of the meander, and bottlenecks, responsible for lower critical current values and detected counts (see result section). Nevertheless, this should verified a posteriori with the use of SEM imaging.

The kinetic inductance or, equivalently, the pulse time constant are obtained for analogous reasons. The kinetic inductance value should fall within a reference window, which typically goes from 50 nH to 200 nH. Indeed, Larger values of the kinetic inductance are associated with small count rates while smaller ones will induce positive electro-thermal feedback (latching of the device), thus not allowing the recovery of the superconducting state upon photon detection. The waveform of the detected signal is also studied to understand if the system is latching during the experiment. This can be done only if the device under investigation shows counts. Latching devices will exhibit a very long time constant consistent with the lack of recovery of the superconductive state. Fig7.6 shows the electrical pulse detected from the oscilloscope and Fig7.7 its exponential fitting. The

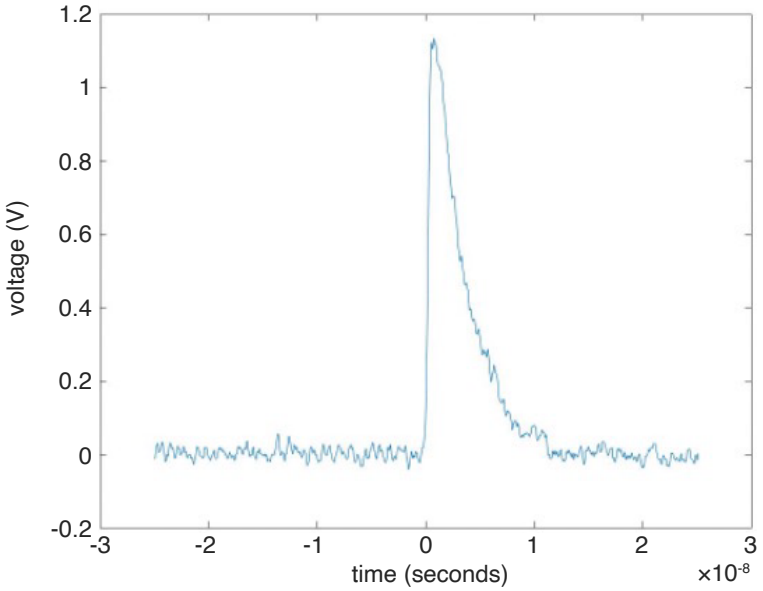

Figure 7.6: Detected pulse

exponential fit shown in 7.7 is performed through python. Two parameters a and b of the following equation are optimized in order to retrieve the correct shape of the decaying

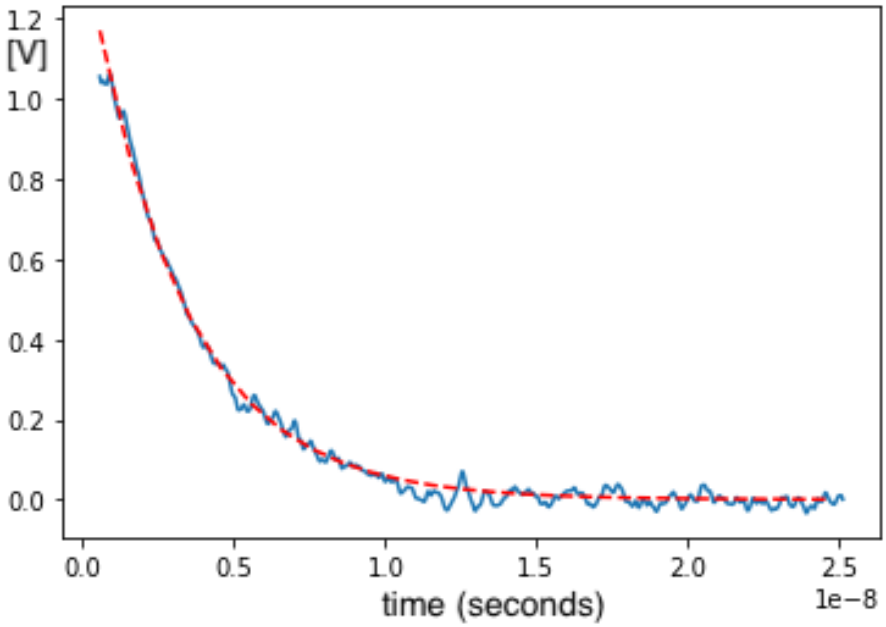

Figure 7.7: Exponential fit of the pulse waveform

pulse.

$$y = a * \exp b * t; \tag{7.3}$$

Y is a vector of voltage values and t is a vector of time values. The time constant, obtained as the reciprocate value of b=317767803.39 is τ= 3,14 ns and thus the kinetic inductance is L_K=157,34 nH. The latter one is obtained just by multiplying the time constant for the load resistance as seen in previous equations. The kinetic inductance is in the correct working range.

7.3. Results

In the previous section the modalities that had been adopted to discard non working devices were argued. The results provided in this section thus only refer to devices which exhibit good parameter values. The results for flood illumination at $\lambda = 850$ nm using NbTiN SNSPDs on SiO_2 substrates are presented. As in the same chip many SNSPDs can be fabricated but a maximum number of eight devices can be measured each time, the same chip needs to be loaded into the cryostat several times. A total of four experiments and and 27 devices have been analysed. The first experiment regards the devices in Fig.1 (see Appendix B) where just three devices, two of which characterised by a width of 150 nm and one by a width of 100 nm, could be measured (150 nm highlighted in the figure). Such SNSPDs showed no counts under light illumination and very few dark counts, with an average of 2 cps (counts per second). This is interpreted as a first evidence that the threshold for $\lambda = 850$ nm is below 100 nm.

The second layout is analogous to the first one, but the designs are restricted to kinetic inductances ranging from a minimum value L_K of 100 nH to a maximum value L_K of 250 nH. This design contains interleaved structures as well, whose purpose is to detect "cross talk", i.e., quantum interaction mechanisms, between the two SNSPDs at a very short distance (around 70 nm). The overall image is reported in chapter 2 in Fig.2.3 and Fig.2.1. The extracted parameters of tested SNSPDs are summarized in Fig.7.8. It might

	J1	J2	J3	J4	J5	J6	J7	J8
RT-Res.(Kohm)	11	1070	12.7	423	104	16.5	325	46.3
W(nm)	150	200	200	150	100	70	100	70
l(um)	375	500	200	150	250	175	100	70
Channel	4	2	7	3	8	6	1	5
I_c (ill-noill) (uA)					43-47.13	32-49	47-58	33-47.5
I_b,max (uA)					40			
Color					cyan	yellow	blue	purple
L(expected Kinetic inductance) (nH)					250	250	100	100
Time costant (ns)					3,68 ns			
Measured kinetic inductance (nH)					186			

Figure 7.8: Tested devices in the second experiment

be noticed that two values for the critical current are reported: the one recorded under no illumination and the one under illumination conditions. The reliable value is the first one because, as the critical current is temperature dependent, under flood illumination the nanowire will heat up thus leading to a different value of Ic.
The devices J2, J4, J5 and J7 are considered to be the only reliable ones as they present a correct value for the room temperature resistance. J5 (w=100 nm) and J7 (w=100 nm) both exhibit very few counts and dark counts as shown, respectively, in Fig7.9 and in

Fig7.10, while J2 (w=200 nm) and J4 (w=150 nm) exhibit none. This result is a further

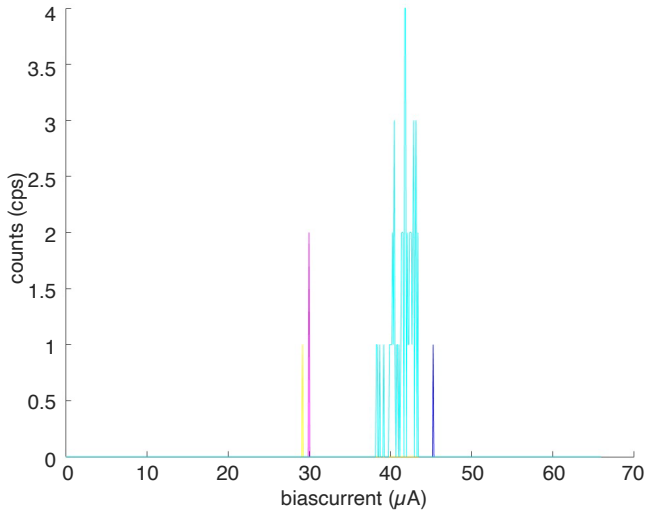

Figure 7.9: Detected counts

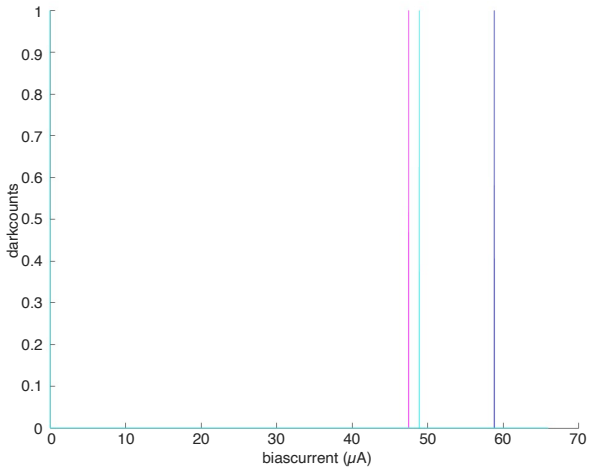

Figure 7.10: Dark counts

evidence that the threshold for $\lambda = 850$ nm detection in NbTiN SNSPD devices should be for width barely lower than 100 nm.

The last two experiments are carried out using the same chip. The devices are shown in Fig.2 and in Fig.3 of the Appendix B. In this case, to fabricate the chip different electron beam doses have been applied. Four replicas with four different and increasing doses [175-183.75-192.5-201.25] mJ/cm^2 are fabricated.

	J1	J2	J3	J4	J5	J6	J7	J8
RT-Res.	650 kohm	25,36 kohm	0,52 Mohm	1, 26 Mohm	230 kohm	1,24 Mohm	470 kohm	1,08 Mohm
W(nm)	150	70	70	70	150	100	200	150
l(um)	375	420	70	175	150	250	200	375
Channel	8	4	1	3	2	6	7	5
I_c (ill-noill) (uA)	29	25	no	32	52.5	no	43.5	52
I_b,max (uA)	24			30				
Color	cyan	cyan	no	red	green	no	black	purple
L(expected Kinetic inductance) (nH)	250	600	100	250	100	250	100	250
Time costant (ns)	2,12			2,82				
Measured kinetic inductance (nH)	106			141				

Figure 7.11: Tested devices in the third experiment

Experiment three is performed with the devices reported in the table Fig.7.11. Under this circumstance, all room temperature resistances fall in the good value range with the exception of J2, which is discarded. J3, instead, is not considered due to the fact that it exhibits no critical current in the region of investigation, which is inconsistent if compared to devices having the same width. The reasons for such choice are better explained in the previous section. Overall we thus consider J1, J4, J5, J6, J7 and J8. All these devices show no counts under illumination with the exception of J1 and J4 which have a width of, respectively, 150 nm and 70 nm. We conclude that the detection threshold should fall within these devices widths, thus around 100 nm. Nevertheless, as it was discussed in the previous section J1 is not considered entirely reliable for both critical current and room temperature resistance values (see previous discussion for further details). This argument is further supported if we consider that detected counts for J1 are relevantly more than for J4.

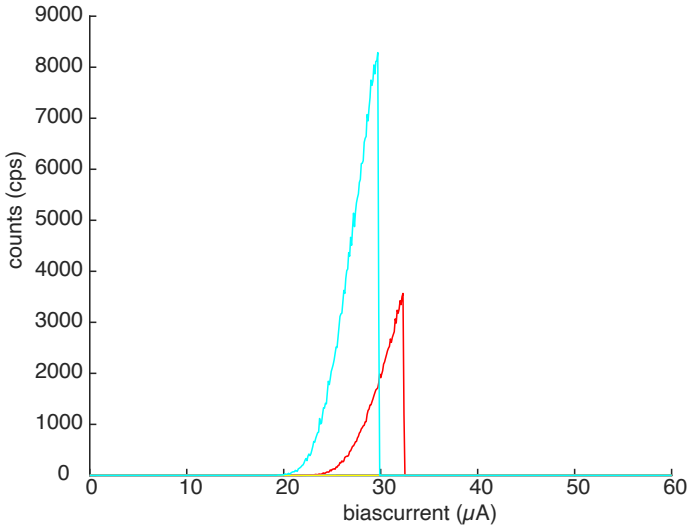

Figure 7.12: Detected counts

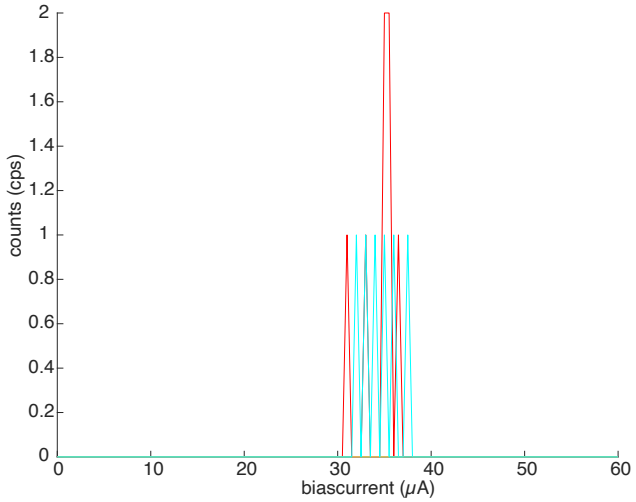

Figure 7.13: Dark counts

The final experiment is carried out on a different set of SNSPDs making part of the same chip. The chosen SNSPDs are reported in table 7.14. All reported devices have

	J1	J2	J3	J4	J5	J6	J7	J8
RT-Res.	460 kohm	1.5 Mohm	0,52 Mohm	480 kohm	230 kohm	1,24 Mohm	470 kohm	1,08 Mohm
W(nm)	200	70	70	100	150	100	200	150
l(um)	200	245	70	100	150	250	200	375
Channel	4	2	1	3	8	6	5	7
I_c (ill-noill) (uA)	48.5	36-34.5	41-36.5	49-34	34-31	no	43	no
I_b,max (uA)	no	33	no	no	no	no	no	no
Color	cyan	green	blue	red	cyan	no	fuchsia	no
L(expected Kinetic inductance) (nH)		350						
Time costant (ns)		5,49						
Measured kinetic inductance (nH)		274						

Figure 7.14: Tested devices in the fourth experiment

a reasonable value for the room temperature resistances. J6 and J8 are not considered as they exhibit no superconducting behavior (see voltage to bias current characteristic reported in the previous section). The figure concerning counting under illumination condition and dark counts are reported in Fig.7.12 and Fig.7.13

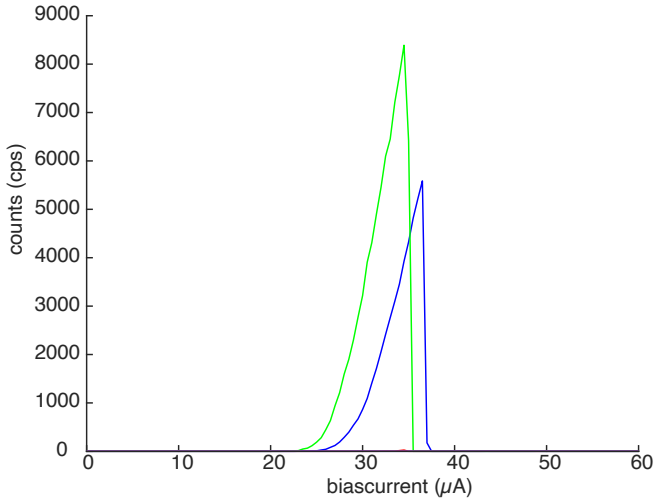

Figure 7.15: Detected counts

This last experiment brings further evidence to the conclusions that were previously reached. Indeed just SNSPD devices with 70 nm width detect the IR light (highlighted in the table), while all the others show no counts.

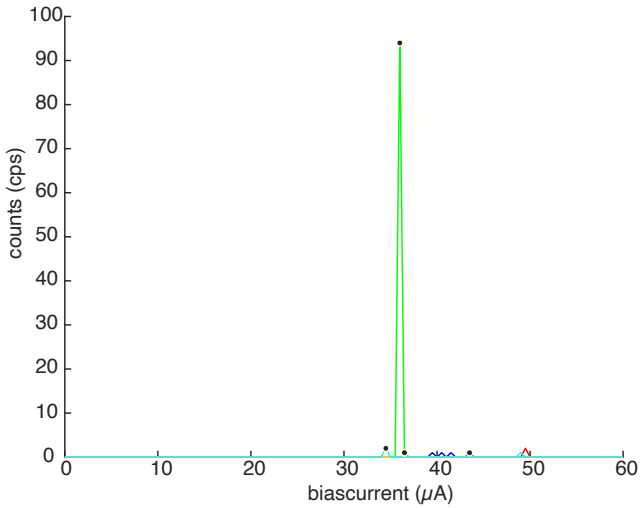

Figure 7.16: Dark counts

To sum up, a total of four experiments and 27 devices have been analysed. Just 19 out of 27 devices showed parameters within the suitable ranges. The results counts are summarized in the following The only devices showing relevant (>10 kcps) counts have a

Widths (nm)	70	100	150	200
Tested devices	3	4	8	4
No counts		3	7	4
1cps < counts < 10 cps		1		
10 cps < counts < 1 kcps				
1 kcps < counts < 10 kcps	3		1	

Figure 7.17: Result scheme

width of 70 nm. Just few counts are detected by one device having 100 nm width. We conclude that the width threshold for $\lambda = 850$ nm light detection for NbTiN SNSPDs of 12 nm thickness is close to 100 nm. Nevetheless, an exception is represented by the red squared of the previous figure where a 150 nm device exhibit 9000 cps. As it was discussed in the previous section such device shows weakly inconsistent parameters from the comparison with other device and so it should not be considered entirely reliable.

It is therefore possible to use 100 and 150 nm (it is safer to use the second value) wide devices to perform again the experiment carried out in [2]. With such devices we expect a relevant reduction in the detection events coming from substrate scintillation (Quartz),

if substrate scintillation is found to largely contribute to secondary detection emission in X-ray SNSPDs. Equivalently, it is possible to employ the same layout as the one we used for this thesis work. Exhibiting several widths at the same time and being the threshold for detection within such widths, this layout will give us the possibility to compare devices showing just both direct detection mechanism with devices showing only indirect detection mechanism. From this, we will be able to estimate the substrate scintillation contribution.

As far as interleaved structures are concerned, to which the channels J1 and J2 refers, they show no cross talk mechanism. The investigation of the interaction between the inner and outer device of the interleaved design is performed. First the internal device is biased and detection events of both structures are recorded. Then the external one is biased and again detection events of both structures are recorded. The results show that no detection mechanism takes place in the unbiased device.

7.4. Scanning electron microscope (SEM) imaging

A scanning electron microscope (SEM) (FEI Nova 200) is a type of electron microscope that produces images of a sample by scanning the surface with a focused beam of electrons. The electrons interact with atoms in the sample, producing various signals that contain information about the surface topography and composition of the sample. Back-scattered electron (BSE) imaging is commonly employed, which relies on electrons originating from a broad region within the interaction volume, or to obtain more surface sensitive secondary electrons (SE) imaging mode can also be used. Secondary electrons originate from the surface or the near-surface regions of the sample. They are a result of inelastic interactions between the primary electron beam and the sample and have lower energy than the backscattered electrons. For these reasons secondary electrons are very useful for the inspection of the topography of the sample surface. This tool can be used to further characterise our devices. In particular, it can be used to find evidence of the fabrication imperfections we inferred in the previous section. In the first experiment just three devices out of 12 showed a room temperature resistance while all the others saturated. This is confirmed by SEM image which reports delamination during nanowire patterning. Fig.7.18 shows resist delamination during nanowire patterning

Fig.7.19 shows underexposure of the 70 nm (J3 in the third experiment) device as the space in between the hairpin is wider than the wire width (these two widths should be identical). Underexposure is further supported by the fact that the nanowire width appears even wider through SEM imaging. Indeed, as SEM exploits an electron beam to allow for such great resolution, non-conductive samples undergo charge accumulation

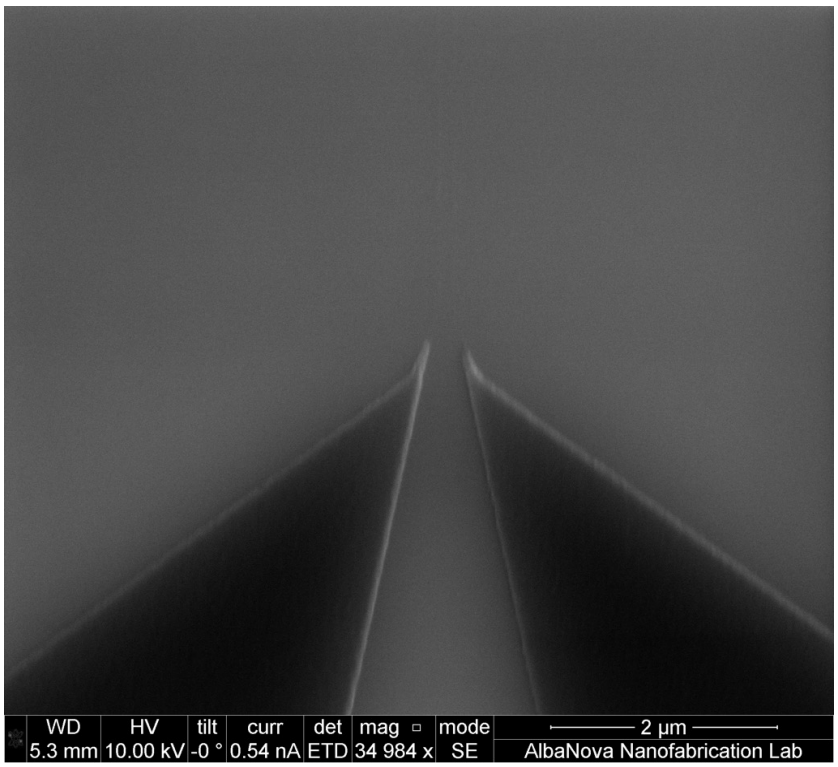

Figure 7.18: Sem image of resist delamination during nanowire patterning

effect. This means that non-conductive specimens collect charge when scanned by the electron beam, and especially in secondary electron imaging mode, it causes scanning faults and other image artifacts. For conventional imaging in with SEM, specimens must be electrically conductive, at least at the surface, and electrically grounded to prevent the accumulation of electrostatic charge. Although the NbTiN is conductive, the resist which remains attached to side walls of the nanowire is not. Fig.7.19 shows a SEM (scanning electron microscope) image of the SNSPD.

Fig.7.20 shows the SEM image of a 70 nm wide and 175 μm long device (J6 in the second experiment, see previous section). The black coloured portions within the hairpin width (same colour as the device) represent resist that was not properly developed. This implies that NbTiN underneath was not properly etched, resulting in a short-circuited device.

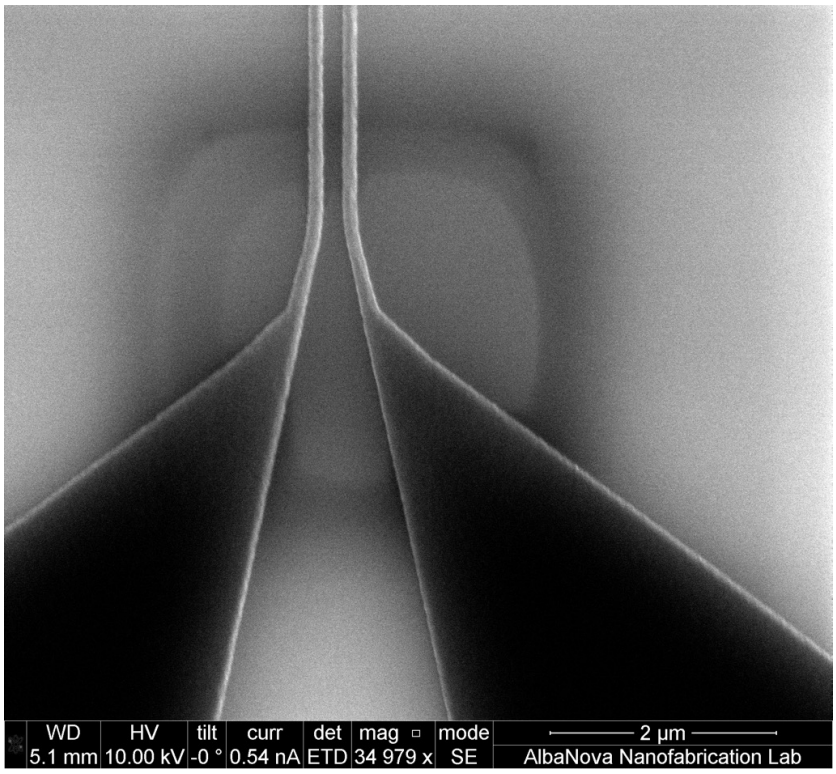

Figure 7.19: SEM image of underexposed features of a 70 nm device

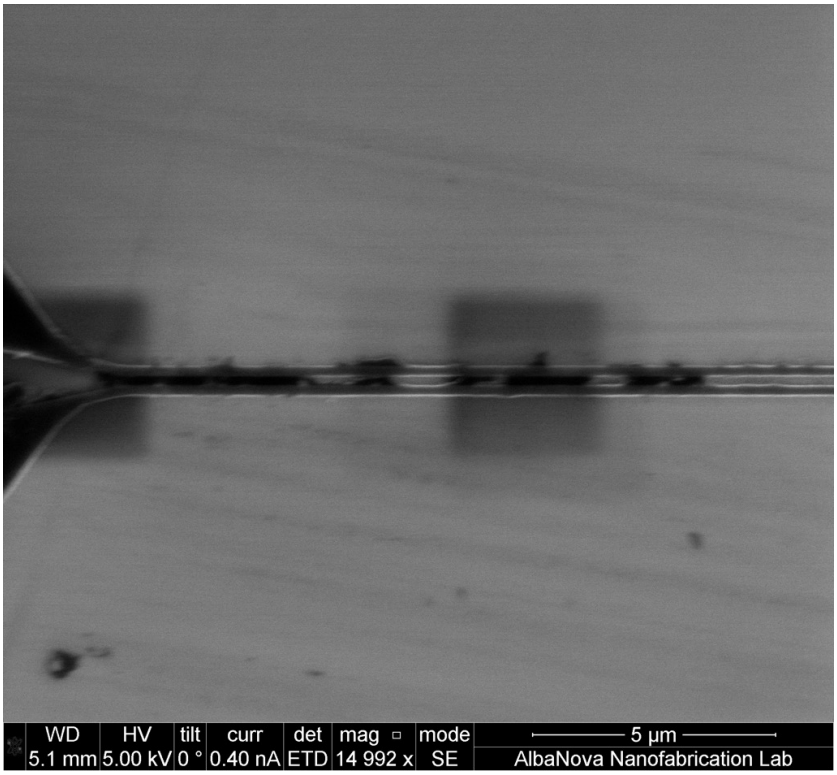

Figure 7.20: Sem image of 70 nm width device (J6 in the table above)

8 | Conclusions and future developments

Superconducting nanowire single-photon detectors exhibit highly relevant properties when operating in the infrared regime. Almost unity detection efficiency, large maximum count rate and low time jitter make these devices suitable for a considerable number of applications. In addition, as they rely on two different detection mechanisms, SNSPDs can be employed for wavelengths ranging from the mid-infrared to the X-ray, increasing further the number of applications. Nevertheless, SNSPDs response in the X-ray range is still not sufficiently investigated and the detection mechanism still not fully understood. This work is intended to address this need. In particular, the purpose of this thesis project is to investigate the relevance of the substrate scintillation mechanism in the X-ray indirect detection mechanism of SNSPDs. Devices with different widths have been fabricated and tested to achieve complete suppression of visible-infrared counts (substrate scintillation range), in particular at a wavelength of $\lambda = 850$ nm. Such wavelength was used to simulate SiO_2 X-ray induced scintillation. Results show that the threshold for such wavelength detection is included in the 70-100 nm width range. This result allows us to infer that many fewer detection events will be obtained if an analogous experiment as in [2], i.e., with an X-ray source is performed. Such an experiment was indeed meant to be carried out. During my thesis experience in Stockholm, much effort was placed in setting up a laboratory with almost all the necessary equipment. Unfortunately, due to bureaucratic reasons, this second experiment was delayed.

Future developments: Finally, the future developments of this project are twofold. On the one hand, if substrate scintillation is found to be the most relevant indirect detection responsible in SNSPDs, future investigations in the X-ray range should look at substrate engineered detectors. In particular, understanding the energy range of the incoming X-rays could be done by taking advantage of the substrate. On the other hand other geometries can be investigated. An example concerns horizontally hit detectors with a length greater than the penetration depth of the incoming x-rays. In this way it will be

possible to address SNSPD direct detection in the X-ray range and compare its efficiency with the indirect one.

Bibliography

[1] V.B. Verma. Single-photon detection in the mid-infrared up to 10 m wavelength using tungsten silicide superconducting nanowire detectors. *APL Photonics*, 2021.

[2] Julien Zichi Iman E. Zadeh Stephan Steinhauer Val Zwiller Artur Branny, Pierre Didier and Ulrich Vogt. X-ray induced secondary particle counting with thin nbtin nanowire superconducting detector. *IEEE TRANSACTIONS ON APPLIED SUPERCONDUCTIVITY*, 2021.

[3] M Ejrnaes2 L Parlato A Sannino A Boselli G P Pepe R Cristiano D Salvoni1, 2 and X Wang. Lidar techniques for a snspd-based measurement. *Journal of Physics*, 2019.

[4] Patrick Eraerds; Matthieu Legre; Jun Zhang; Hugo Zbinden; Nicolas Gisin. Photon counting otdr: Advantages and limitations. *Journal of Lightwave Technology*, 2009.

[5] Chao Wan Junhui Hu Tao Jia Min Gu Labao Zhang Lin Kang Jian Chen Xuping Zhang Peiheng Wu Qingyuan Zhao, Lan Xia. Long-haul and high-resolution optical time domain reflectometry using superconducting nanowire single-photon detectors. *Scientific Reports*, 2015.

[6] John O Prior Dimitris Visvikis Stefan Gundacker Etiennette Auffray Peter Križan Rosana Martinez Turtos Dominique Thers Edoardo Charbon Paul Lecoq, Christian Morel. Roadmap toward the 10 ps time-of-flight pet challenge. *Physics in Medicine Biology*, 65, 2020.

[7] Johannes W. N. Los Samuel Gyger Ali W. Elshaari Stephan Steinhauer Sander N. Dorenbos Iman Esmaeil Zadeh, J. Chang and Val Zwiller. Superconducting nanowire single-photon detectors: A perspective on evolution, state-of-the-art, future developments, and applications. *Applied Physics letter*, 2021.

[8] Sae Woo Nam Richard P. Mirin Dileep V. Reddy, Robert R. Nerem and Varun B. Verma. Superconducting nanowire single-photon detectors with 98% system detection efficiency at 1550nm. *Optica*, 7:1649–1653, 2020.

[9] J. O. Tenorio-Pearl N. Noordzij R. Gourgues A. Guardiani J. R. Zichi S. F. Pereira

H. P. Urbach V. Zwiller S. N. Dorenbos J. Chang, J. W. N. Los and I. Esmaeil Zadeh. Detecting telecom single photons with (99.5+0.52.07) % system detection efficiency and high time resolution. *APL Photonics*, 2021.

[10] Hiroki Takesue Hiroyuki Shibata, Kaoru Shimizu and Yasuhiro Tokura. Ultimate low system dark-count rate for superconducting nanowire single-photon detector. *Optics Letters*, 40:3428–3431, 2015.

[11] K. Makise W. Qiu H. Terai M. Fujiwara M. Sasaki T. Yamashitaa, S. Miki and Z. Wang. Origin of intrinsic dark count in superconducting nanowire single-photon detectors. *Applied Physics letter*, 2011.

[12] Sonia M. Buckley et al. Adam N. McCaughan, Alexander N. Tait. Phidl: Python-based layout and geometry creation for nanolithography. *J. Vac. Sci. Technol*, 2021.

[13] John R. Clem and Karl K. Berggren. Geometry-dependent critical currents in superconducting nanocircuits. *PHYSICAL REVIEW B*, 2011.

[14] Samuel Gyger Thomas Lettner Carlos Errando-Herranz Klaus D. Jons Mohammad Amin Baghban Katia Gallo Julien Zichi Stephan Steinhauer, Lily Yang and Val Zwiller. Nbtin thin films for superconducting photon detectors on photonic and two-dimensional materials. *Applied Physics letter*, 2020.

[15] Stephan Steinhauer et al. Julien Zichi, Jin Chang. Optimizing the stoichiometry of ultrathin nbtin films for high-performance superconducting nanowire single-photon detectors. *Optics express*, 2019.

[16] Sami Franssila. *Introduction to Microfabrication*. John Wiley Sons, second edition, 2010.

[17] Buno López Rodríguez. Towards the detection of single photons in the mid- infrared. Master's thesis, KTH, 2021.

[18] Magnus Andersson. Superconductivity - module 1. Technical report, Royal Institute of Technology, 2020.

[19] Magnus Andersson. Superconductivity - module 2. Royal Institute of Technology, Stockholm, Sweden, 2020.

[20] Magnus Andersson. Superconductivity - module 3. Technical report, Royal Institute of Technology, Stockholm, 2020.

[21] K.E.Gray andR.G.Wagner Alberto Gabutti. Granular-aluminum superconducting

detector for 6 kev x-rays and 2.2mev beta sources. *NationalInstituteofStandard-sandTechnology*, 1989.

[22] I. Florya A. Semenov R. Espiau de Lamastre P. Cavalier G. Gol'tsman J.-P. Poizat L. Maingault, M. Tarkhov and J.-C. Villgier. Spectral dependency of superconducting single photon detectors. *JOURNAL OF APPLIED PHYSICS*, 2010.

[23] M. Borysiewicza R. Kruszkaa Z. Sidora M. Juchniewicza K. Golaszewskaa J.Z. Domagalaa b-W. Rzodkiewicza J. Ratajczaka J. Bara M. Wegrzeckia M. Guziewicza, W. Slysza and R. Sobolewskia. Technology of ultrathin nbn and nbtin films for superconducting photodetectors. *ACTA PHYSICA POLONICA A*, 2011.

[24] S. Dobrovolskiy S. N. Dorenbos V. Zwiller E. Monroy L. Redaelli, G. Bulgarini and J. M. Gerard. Design of broadband high-efficiency superconduct- ing-nanowire single photon detectors. *Supercond. Sci. Technol.*, 2016.

[25] Karl K. Berggren et al. Experimental methods in the physical sciences. *ScienceDirect*, 2013.

[26] Taeyoon Hong et al. Terahertz electrodynamics and superconducting energy gap of nbtin. *Journal of Applied Physics*, 2013.

[27] Lixing You. Superconducting nanowire single-photon detectors for quantum information. *Nanophotonics*, 2020.

[28] E. E. Kohnke P. J. Alonso, L. E. Halliburton and R. S. Sossoli. X-ray-induced luminescence in crystalline si02. *Journal of Applied Physics*, 1983.

[29] Lixing You Heqing Wang You Xiao Jia Huang Xiaoyan Yang Weijun Zhang Zhen Wang Peng Hu, Hao Li and Xiaoming Xie. Detecting single infrared photons toward optimal system detection efficiency. *Optics Express*, 2020.

[30] R. Meservey and P. M. Tedrow. Measurements of the kinetic inductance of superconducting linear structures. *Journal of Applied Physics*, 2003.

[31] Luigi Frunzio1 Gianluigi Catelani Michael J Rooks Aviad Frydman Anthony J Annunziata1, Daniel F Santavicca1 and Daniel E Prober. Tunable superconducting nanoinductors. *IOP PUBLISHING - Nanotechnology*, 2010.

[32] Eric A. Dauler Andrew J. Kerman, Joel K. W. Yang William E. Keicher, Karl K. Berggren G. Gol'tsman, and B. Voronov. Kinetic-inductance-limited reset time of superconducting nanowire photon counters. *APPLIED PHYSICS LETTERS*, 2006.

[33] 2 Richard J. Molnar 1 Eric A. Dauler 1 2 Andrew J. Kerman, 1 Joel K. W. Yang

and Karl K. Berggren2. Physical review b 79, 100509r 2009 electrothermal feedback in superconducting nanowire single-photon detector. *PHYSICAL REVIEW B*, 2009.

[34] W.H.P.Pernice C.Schuck and H.X.Tang. Waveguide integrated low noise nbtin nanowire single-photon detectors with milli-hz dark count rate. *Sci. Rep*, 2013.

[35] A.Schilling K.Il'in K.Inderbitzin, A.Engel and M.Siegel. An ultra-fast superconducting nb nanowire single-photon detector for soft x-rays,. *Applied Physics letter*, 2012.

[36] Wang Qiang Schilling Andreas Zhang, Xiaofu. Superconducting single x-ray photon detector based on w 0.8 si 0.2. *AIP advances*, 2016.

A | PHIDL code

```
import phidl.geometry as pg
from scipy.optimize import fminbound
from phidl import quickplot as qp
from phidl import Device
import numpy as np
import phidl.routing as pr
Enclosedstructure1 = Device('SNSPD')
V = Device('Label')
S = Device('SNSPD')
C = Device('conn')
Ct = Device('connt')
Cv = Device('connv')
C1 = pg.arc(radius = 2.0, width = 0.07, theta = 7, start_angle = 0,
angle_resolution = 2.5, layer = 0)
C2 = pg.optimal_step(start_width = 0.07, end_width = 15, num_pts = 100,
width_tol = 1e-3, anticrowding_factor = 1.1, symmetric = False, layer = 0)
conn1_ref = Ct.add_ref(C1)
C3 = pg.optimal_step(start_width = 15, end_width = 150, num_pts = 100,
width_tol = 1e-3, anticrowding_factor = 0.35, symmetric = False, layer = 0)
conn2_ref = Ct.add_ref(C2)
conn3_ref = Cv.add_ref(C3)
conn2_ref.move([100,0])
P = pg.compass(size = (150,150), layer = 0)
pad_ref1 = Cv.add_ref(P)
conn2_ref.connect(port = 1, destination = conn1_ref.ports[2] )
Ct.add_port(name = 1, port = conn1_ref.ports[1])
Ct.add_port(name = 2, port = conn2_ref.ports[2])
```

```
qp(Ct)
conn3_ref.connect(port = 2, destination = pad_ref1.ports['W'] )
Cv.add_port(name = 1, port = conn3_ref.ports[1])
Cv.add_port(name = 2, port = pad_ref1.ports['E'])
qp(Cv)
Cv_ref = C.add_ref(Cv)
Ct_ref = C.add_ref(Ct)
qp(C)
Cv_ref.connect(port = 1, destination = Ct_ref.ports[2] )
qp(C)
C.add_port(name = 1, port = Ct_ref.ports[1])
C.add_port(name = 2, port = Cv_ref.ports[2])
qp(C)
H = pg.optimal_hairpin(width = 0.07, pitch = 0.14, length = 200,
    turn_ratio = 20, num_pts = 50, layer = 0)
qp(H)
Cup_ref =S.add_ref(C)
qp(C)
Cdown_ref = S.add_ref(C)
hairpin_ref = S.add_ref(H)
Cup_ref.move([0,100])
Cup_ref.mirror(p1=[0,0], p2=[0,5])
Cdown_ref.mirror(p1=[0,0], p2=[5,0])
Cdown_ref.mirror(p1=[0,0], p2=[0,5])
Cdown_ref.move([0,-100])
qp(S)
Cup_ref.connect(port = 1, destination = hairpin_ref.ports[1] )
qp(S)
Cdown_ref.connect(port = 1, destination = hairpin_ref.ports[2] )
S.move([245,0])
Label_ref = S.add_label(text='L=285 l=200 w=0.07', position=(-150, 0),
magnification=70, rotation=None, anchor='o', layer=255)
V = pg.text(text = 'L=285 l=200 w=0.07' , size = 50, justify = 'left', layer = 0)
realabel_ref = S.add_ref(V)
V.move([-320,500])
qp(S)
A = Device() # Create a new blank Device
```

```
d_ref1 = A.add_array(S, columns = 1, rows = 1, spacing = [2000,0])
# Reference the Device "D" that 3 references in it
A.move([-170,0])
qp(A)
# Quickplot the reference-containing device "D"
first_ref = Enclosedstructure1.add_ref(A)
```

B | Experiment designs

Designs for experiment 1:

Figure 1: First experiment

Designs for experiments 3 and 4 :

Figure 2: Designs with ebl (electron beam lithography) dose of 192.5 mJ/ cm^2(left) 201.25 mJ/ cm^2 (right)

Figure 3: Designs with ebl (electron beam lithography) dose of 175 mJ/ cm^2(left) 183.75 mJ/ cm^2 (right)

List of Figures

List of Tables

List of Symbols

Variable	Description	SI unit
$\boldsymbol{u}$	solid displacement	m
$\boldsymbol{u}_f$	fluid displacement	m

Acknowledgements

I would like to thank my supervisor Stephan Steinhauer without whom this project would not have been possible and my professors Gianluca Valentini, Val Zwiller and Ulrich Vogt for giving me this great opportunity.